Published in final edited form as:
J Geophys Res Biogeosci. 2016 February ; 121(2): 312–336. doi:10.1002/2015JG003031.

Dissolved organic carbon fluxes in the Middle Atlantic Bight: An integrated approach based on satellite data and ocean model products

Antonio Mannino[1], **Sergio R. Signorini**[1,2], **Michael G. Novak**[1,3], **John Wilkin**[4], **Marjorie A. M. Friedrichs**[5], and **Raymond G. Najjar**[6]

[1]NASA Goddard Space Flight Center, Greenbelt, Maryland, USA

[2]Science Applications International Corp., Washington, District of Columbia, USA

[3]Science Systems and Applications Inc., Lanham, Maryland, USA

[4]Institute of Marine and Coastal Sciences, State University of New Jersey Rutgers, New Brunswick, New Jersey, USA

[5]Virginia Institute of Marine Science, College of William and Mary, Gloucester Point, Virginia, USA

[6]Department of Meteorology, Pennsylvania State University, University Park, Pennsylvania, USA

Abstract

Continental margins play an important role in global carbon cycle, accounting for 15–21% of the global marine primary production. Since carbon fluxes across continental margins from land to the open ocean are not well constrained, we undertook a study to develop satellite algorithms to retrieve dissolved organic carbon (DOC) and combined these satellite data with physical circulation model products to quantify the shelf boundary fluxes of DOC for the U.S. Middle Atlantic Bight (MAB). Satellite DOC was computed through seasonal relationships of DOC with colored dissolved organic matter absorption coefficients, which were derived from an extensive set of in situ measurements. The multiyear time series of satellite-derived DOC stocks (4.9 Teragrams C; Tg) shows that freshwater discharge influences the magnitude and seasonal variability of DOC on the continental shelf. For the 2010–2012 period studied, the average total estuarine export of DOC into the MAB shelf is 0.77 Tg C yr^{-1} (year). The integrated DOC tracer fluxes across the shelf boundaries are 12.1 Tg C yr^{-1} entering the MAB from the southwest alongshore boundary, 18.5 Tg C yr^{-1} entering the MAB from the northeast alongshore boundary, and 29.0 Tg C yr^{-1} flowing out of the MAB across the entire length of the 100 m isobath. The magnitude of the cross-shelf DOC flux is quite variable in time (monthly) and space (north to south). The highly dynamic exchange of water along the shelf boundaries regulates the DOC budget of the MAB at subseasonal time scales.

Correspondence to: A. Mannino, antonio.mannino@nasa.gov.

Special Section: Carbon and Nitrogen Fluxes at the Land-Ocean Interface

Supporting Information: Supporting Information S1

1. Introduction

Continental margins host large fluxes of carbon, high productivity, and substantial carbon sequestration at levels that are significant to the global carbon cycle and are subject to a disproportionately high impact from climate change and other human activities. Primary production on continental margins comprises 15–21% (9.8 Pg C yr^{-1}; 1 Pg = 10^{15} g; Petagram) of global ocean primary production [*Jahnke*, 2010]. Furthermore, approximately 50–70% of the global biological pump transfer of organic carbon to the seabed occurs in continental margins [*Muller-Karger et al.*, 2005; *Jahnke*, 2010]. Recent estimates of global air-sea CO_2 fluxes suggest that ocean margins are sinks for atmospheric CO_2 (0.25 Pg C yr^{-1} or 17% of global uptake) with low-latitude margins as sources and middle- to high-latitude margins as sinks [*Cai*, 2011]. Globally, rivers export an estimated but variable 0.45 Pg organic carbon per year to continental margins with dissolved organic carbon (DOC) comprising nearly 55% of the total [*Meybeck*, 1993; *Cai*, 2011; *Bauer et al.*, 2013]. DOC alone comprises over 80–90% of the organic carbon found in the coastal ocean [e.g., *Bates and Hansell*, 1999] and constitutes one of the largest pools of organic carbon in the biosphere [*Hedges*, 2002]. *Bauer et al.* [2013] estimated the global export of DOC from continental margins to the open ocean at 0.15–0.35 Pg C yr^{-1} with an uncertainty greater than 100%. Despite the important role of continental margin DOC to the global carbon cycle and as a source of energy and nutrients to aquatic organisms, only a few studies have investigated DOC fluxes and stocks within continental margins [*Chen and Wang*, 1999; *Vlahos et al.*, 2002; *de Madron et al.*, 2003; *Hung et al.*, 2003; *Liu et al.*, 2014]. These studies have demonstrated that significant DOC exchange occurs along the continental shelf and slope boundaries with the open ocean and across adjacent margins.

DOC correlates strongly with colored dissolved organic matter (CDOM) absorption coefficient (a_{CDOM}) for many coastal and inland waters including rivers, estuaries, and continental margins [e.g., *Ferrari et al.*, 1996; *Vodacek et al.*, 1997; *Del Castillo et al.*, 1999; *Stedmon et al.*, 2000; *Mannino et al.*, 2008; *Fichot and Benner*, 2011; *Spencer et al.*, 2012]. This permits satellite retrievals of DOC from satellite-derived a_{CDOM} [*Del Castillo and Miller*, 2008; *Mannino et al.*, 2008; *Griffin et al.*, 2011; *López et al.*, 2012; *Liu et al.*, 2014]. Satellite-derived DOC distributions have also been applied to quantify DOC stocks on continental margins [*Mannino et al.*, 2008; *Liu et al.*, 2014], fluxes of DOC from rivers to the continental shelf [*Del Castillo and Miller*, 2008; *López et al.*, 2012] and net community production of DOC [*Mannino et al.*, 2008]. The key advantage afforded by ocean color satellite sensors is the provision of near-surface ocean observations at more detailed spatial and temporal distributions than possible with field sample collections alone. A limitation is that these observations are available only near the surface, i.e., the first optical depth.

Numerous field studies conducted over the past several decades in the U.S. Middle Atlantic Bight (MAB) offer a wealth of information on the physics, ecology, and biogeochemical processes of this region. The MAB is located along the continental margin of the U.S. East Coast and extends customarily from Cape Cod, Massachusetts, to Cape Hatteras, North Carolina. The Shelf Edge Exchange Processes experiments (SEEP I and SEEP II) [*Biscaye et al.*, 1994] and the Ocean Margins Program (OMP) [*Verity et al.*, 2002] in particular focused on carbon flow within the MAB. From the SEEP experiments, primary production

in the MAB was estimated to be 75 Tg C yr^{-1} (1 Tg C = 10^{12} g C), and only 4.8 Tg C yr^{-1} of the annual production on the shelf was estimated to be exported off the shelf as particulate organic carbon [*Falkowski et al.*, 1988; *Anderson et al.*, 1994; *Falkowski et al.*, 1994]. DOC was not studied under the SEEP program. As part of OMP, *Vlahos et al.* [2002] utilized DOC profiles from multiple cruises to develop a DOC budget for the MAB including estimates of DOC stock (~6 Tg C) and cross-shelf DOC export (~19 Tg C yr^{-1}) from the MAB to the open ocean. DOC concentrations ranged from 55 to 177 μM C with higher concentrations near river/estuary outflows and lower concentrations within outer shelf and slope waters of the northeast region of the MAB [*Vlahos et al.*, 2002]. However, the temporal and spatial distributions of these and other carbon measurements were insufficient to quantify the seasonal and inter-annual variability of carbon fluxes and inventories within continental margins of this size and complexity. Although three-dimensional biogeochemical models coupled to physical models have made significant progress in characterizing carbon budgets within the MAB [e.g., *Fennel et al.*, 2008; *Druon et al.*, 2010; *Hofmann et al.*, 2008, 2011], further work is needed to accurately reproduce the magnitude and spatial-temporal dynamics of DOC. As a complementary approach to coupled models, *Signorini et al.* [2013] applied field measurements and satellite data to quantify the partial pressure of CO_2 and air-sea fluxes of CO_2 for coastal waters of eastern North America, including the MAB, which was found to be a sink for atmospheric CO_2 (2.1 Tg C yr^{-1}).

For this study, we applied field measurements of DOC, temperature and salinity, satellite retrievals of DOC, a machine-learning model to compute the vertical profiles of DOC, and outputs from a physical circulation model to quantify the DOC stocks and boundary fluxes for the MAB and investigate their seasonal and inter-annual variability. Our objectives were (1) to develop and validate DOC algorithms for the MAB and its major estuaries, (2) to develop and evaluate a neural network model to predict DOC vertical profiles, (3) to investigate the seasonality of the DOC stocks in the MAB shelf, and (4) to quantify the horizontal boundary DOC fluxes on the continental shelf using an integrated tracer flux approach.

2. Methods

Figure 1 illustrates how field data, statistical models (neural network and regression), satellite data, and physical circulation model products are combined to estimate the four-dimensional estimates of DOC concentrations and fluxes. The spatial resolution of the final product is the same as that of the ocean model (5–6 km in the horizontal) and the temporal resolution is monthly. The temporal extent of the DOC concentration product is 2006–2012, though the flux calculation and most of the analysis is conducted for 2010–2012, based on the availability of physical ocean model output. Field data for DOC, temperature (T), and salinity (S) are fed into a neural network model to estimate the DOC concentration given the latitude, longitude, depth, T, and S. Four-dimensional fields of T and S from the physical ocean model (Regional Ocean Modeling System (ROMS)) are then put through the neural net model to create a 4-D field of DOC, which is then adjusted using a satellite-based estimate of surface DOC determined as follows (see section 2.5). Field data for surface DOC, a_{CDOM}, and reflectance are combined with regression models to relate surface DOC to a_{CDOM} and a_{CDOM} to reflectance. Satellite reflectance estimates and the regression

models are used to create satellite estimates of a_{CDOM} and surface DOC. The satellite-adjusted 4-D fields of DOC are then combined with ROMS estimates of horizontal velocity to compute lateral fluxes. The procedure is presented in more detail after the study region is described.

2.1. Study Region

For this study, the MAB was defined as the region extending from south of Cape Hatteras (~34.5°N) to south of Cape Cod near Georges Bank (~41.5°N) and bounded by the shoreline and the estuary mouths and offshore to the 100 m isobath (Figure 2). The northeastern U.S. continental margin is at the intersection of two large-scale circulation flows: the northward flowing warm Gulf Stream current and the cold southward flowing Labrador slope current. These two currents directly influence the Slope Sea and thereby the adjacent outer shelf of the MAB. The Scotian shelf/slope water, which originates as a buoyancy-driven coastal current (Labrador slope current) that is fed by freshwater flow from melting snow and ice from southern Greenland (~94%) [*Houghton and Fairbanks*, 2001] and outflow from the St. Lawrence River [*Chapman et al.*, 1986; *Chapman and Beardsley*, 1989] promotes the geostrophic counterclockwise surface circulation in the Gulf of Maine [*Brooks*, 1992]. This shelf/slope current then flows into Georges Bank and the MAB, where it drives the alongshore (southward) flow. North of Cape Hatteras the distance between the Gulf Stream and the continental shelf break is variable, which has been ascribed to variations in the flow of Labrador Shelf water into the Slope Sea [*Rossby and Benway*, 2000] or alternatively to changes in wind stress [*Dong and Kelly*, 2003]. These interannual variations in the path of the Gulf Stream, the flow of Labrador water, and river discharge influence biological processes and carbon fluxes along the entire shelf and the shelf-slope front [*Greene and Pershing*, 2007; *Schollaert et al.*, 2004].

In addition to freshwater inputs originating from Labrador shelf water, the MAB receives significant inputs of freshwater from several major river/estuary systems, including Chesapeake Bay, Delaware Bay, Hudson-Raritan Bay, and the Connecticut River. During winter and early spring in the MAB, the alongshore current and northerly winds force estuarine plumes, including Chesapeake Bay [*Rennie et al.*, 1999; *Verity et al.*, 2002], Delaware Bay [*Sanders and Garvine*, 2001], and the Hudson-Raritan plumes [*Johnson et al.*, 2003], to flow southward along the coast and create generally downwelling-favorable conditions. As winds reverse later in spring the southerly alongshore flow weakens. Subsequently, southerly winds of sufficient strength and duration promote upwelling conditions along the MAB during summer [*Glenn et al.*, 2004]. Saline waters from the South Atlantic Bight and the Gulf Stream also intrude into the coastal southern MAB in summer. Consequently, a significant portion of shelf water from the MAB can be advected offshore from the region between Cape Hatteras and Chesapeake Bay [*Churchill and Berger*, 1998; *Verity et al.*, 2002], suggesting that this region is an important site for carbon export to the open ocean [*Bates and Hansell*, 1999; *Vlahos et al.*, 2002]. Warm-core rings generated by landward meanders of the Gulf Stream as well as Gulf Stream filaments and eddies interact vigorously and extensively with the outer-MAB shelf water and entrain and export shelf water and biogeochemical constituents from the MAB shelf to the adjacent deep ocean

[*Garfield and Evans*, 1987; *Lillibridge et al.*, 1990; *Churchill and Cornillon*, 1991; *Joyce et al.*, 1992].

2.2. Field Sampling and Measurements

Field data applied for satellite DOC algorithm development and validation were collected on multiple cruises from May 2004 to February 2013 within the MAB, Gulf of Maine (GoMa), and estuaries of the MAB including Chesapeake Bay, Delaware Bay, and the Hudson-Raritan Estuary (Figure 2). Details for most of the research cruises including dates and areas sampled were described previously [*Mannino et al.*, 2014]. Measurements from two additional cruises conducted within the MAB, GoMa, and Georges Bank areas of the northeastern U.S. continental margin conducted on 7–23 August 2012 (CV7) and 4–26 February 2013 (ECO1) were also included in this study. Data for these and prior cruises were archived in the NASA Sea-viewing Wide Field-of-view Sensor (SeaWiFS) Bio-optical Archive and Storage System (http://seabass.gsfc.nasa.gov/).

2.3. Sample Processing and Analysis

Water samples for the analysis of DOC concentration and a_{CDOM} were collected, processed, and analyzed according to the protocols described in *Mannino et al.* [2008, 2014]. Briefly, CDOM absorbance spectra were measured on a double-beam Cary 100 ultraviolet-visible scanning spectrophotometer using a 100 mm path length quartz cell with ultraviolet oxidized ultrapure water Type I (Milli-Q) as the blank and reference [*Mitchell et al.*, 2003; *Mannino et al.*, 2008, 2014]. DOC was measured by high-temperature combustion oxidation using a Shimadzu TOC-V instrument. Multiple injections (three to seven to maintain a precision of <2%) of replicate samples (two or three replicates) were analyzed along with the deep seawater DOC consensus reference material distributed by Wenhao Chen of Dennis Hansell's Laboratory (Rosenstiel School of Marine and Atmospheric Science, University of Miami, Florida). The utilization of carbon standard calibration curves, check standards, and consensus reference material as well as Milli-Q to estimate the instrument carbon blank [*Benner and Strom*, 1993] yields a measured uncertainty in DOC of 5–6% on average following the methods described in *Mannino et al.* [2008].

2.4. Development of DOC Algorithms and Processing of Satellite DOC

Empirical relationships of DOC to CDOM optical properties from field measurements were investigated to develop and evaluate bio-optical DOC algorithms. Prior studies in the middle and southern MAB [*Mannino et al.*, 2008] and in other coastal regions around the world [*Ferrari et al.*, 1996; *Vodacek et al.*, 1997; *Del Castillo et al.*, 1999; *Stedmon et al.*, 2000; *Fichot and Benner*, 2011] have shown strong correlations between DOC and a_{CDOM}.

The empirical relationships of DOC to CDOM optical properties were evaluated by the least squares approach using the following statistics: the regression coefficient (R^2), the root-mean-square error (RMSE), and visual inspection of the in situ data and the least squares regression curve fit. The Type II linear regression models were used to account for uncertainty in the independent variable (X axis variable). Field data collected from 2004 to 2008 were generally used for in situ bio-optical DOC algorithm development, and data from 2009 to 2013 were applied for satellite validation [*Mannino et al.*, 2014].

Ocean color data used in this study were from the Moderate Resolution Imaging Spectroradiometer (MODIS) and the Sea-viewing Wide Field-of-view Sensor (SeaWiFS). MODIS Aqua and SeaWiFS local area coverage Level 1 files of the study region were obtained from the NASA Ocean Color Web (http://oceancolor.gsfc.nasa.gov/). SeaDAS 6.4 (ocean color satellite data processing software [*Mannino et al.*, 2014]) with standard defaults was applied to process Level 1 files to Level 2. Masks were applied to pixels with any of the followings flags: land, cloud or ice, atmospheric correction failure, high top-of-the atmosphere radiance, low normalized water-leaving radiance at 555 or 547 nm, stray light, or Sun glint, as described in *Bailey and Werdell* [2006]. Validation 3 × 3 pixel arrays centered on the corresponding field station location were extracted from the native resolution satellite data that were collected within 3 h of the in situ sampling [see *Mannino et al.*, 2014]. MODIS Aqua (June 2002 to the present) and SeaWiFS (September 1997 to December 2010) have provided nearly daily coverage of the MAB at 1.0 and 1.1 km near-nadir horizontal resolution, respectively. However, various factors including cloud cover, Sun glint, stray light, edge-of-scan pixel distortions, and imperfect atmospheric corrections reduce the number of valid retrievals for any given “ocean” pixel to approximately one to three observations per week.

Algorithm performance was evaluated by comparing filtered matchup values of coincident satellite-retrieved DOC with field data, which are referred to as validation matchups [*Bailey and Werdell*, 2006; *Mannino et al.*, 2014]. The filtered means for the satellite-derived 3 × 3 pixel arrays were computed using the following formulation:

$$\text{Filtered Mean}=[\textstyle\sum_{\text{i}}(1.5\sigma - X)<x_i<(1.5\sigma+X)]/N \quad (1)$$

where X represents the unfiltered mean value, σ is the standard deviation of the unfiltered values, x_i are the individual values for each pixel array, and N is the number of values from each pixel array that falls within $\pm 1.5\sigma$.

The validation of the DOC algorithms involved several statistical parameters including the mean absolute percent difference (MAPD) and the standard deviation of the MAPD, RMSE, the median ratio of the filtered mean satellite value (DOC_{alg}) to field measurement ($\text{DOC}_{\text{in situ}}$), the percent bias (% Bias), the semi-interquartile range (SIQR), and the R^2 and slope values from linear Type II regression analyses of the validation matchups for each satellite sensor [*Bailey and Werdell*, 2006].

$$\text{MAPD}(\%)=[\textstyle\sum|(\text{DOC}_{\text{alg}} - \text{DOC}_{\text{in situ}})|\text{DOC}_{\text{in situ}}] \times 100/N \quad (2)$$

$$\text{RMSE}(\mu\text{mol L}^{-1}\text{C})=\left[1/N \times \textstyle\sum(\text{DOC}_{\text{alg}} - \text{DOC}_{\text{in situ}})^2\right]^{1/2} \quad (3)$$

$$\mathrm{Bias}(\%)=[(1/N)\times\sum(\mathrm{DOC}_{\mathrm{alg}}-\mathrm{DOC}_{\mathrm{in\ situ}}))/\mathrm{Mean}(\mathrm{DOC}_{\mathrm{in\ situ}})]\times 100 \quad (4)$$

$$\mathrm{SIQR}=(Q_3-Q_1)/2 \quad (5)$$

For the SIQR computation, Q_3 and Q_1 represent the 75th and 25th percentiles for the ratios of the satellite-derived values to the field measurements.

Monthly binned near-surface satellite DOC concentrations were derived from the DOC algorithms developed in this study (section 3.1) from MODIS Aqua Level 3, 4 km daily remote sensing reflectances at 443 and 547 nm (*Rrs*), using the multiple linear regression a_{CDOM} algorithms from *Mannino et al.* [2014]. Satellite DOC was computed for the MAB region by applying the statistically better performing algorithms described in sections 3.1 and 3.2. The MODIS 4 km monthly DOC data for the years 2006–2012 were binned into the coastal ocean model grid. The ocean model products are available at daily time steps and were also binned monthly to match the satellite DOC products.

2.5. Neural Network (NNet) DOC Vertical Profile Model

A model was developed to produce vertical profiles of DOC by relating near-surface values of DOC, which can be obtained from ocean color satellite data, to vertical profiles of *T* and *S* because of the similarity in the shapes of DOC and density vertical profiles. In situ profiles of DOC, *T*, and *S* were obtained from available field data (see section 2.2) and literature [*Guo et al.*, 1995; *Bauer et al.*, 2001, 2002] (see Figure S1 in the supporting information for DOC data). Figure 2 shows the locations of the field data. The DOC vertical profile model was based on the MATLAB function “feedfowardnet.” Feed forward networks consisted of a series of layers. The first layer had a connection from the network input. Each subsequent layer had a connection from the previous layer. The final layer produced the network’s output. Feed forward networks can be used for any kind of input-to-output mapping. In this case, the input consisted of latitude, longitude, depth, *T*, and *S* from field data and the NNet model was trained to reproduce the observed DOC with minimized error. A portion of the data set was used to train the model (~80%), and another portion was used to evaluate its performance (~20%). Here the error for the retrieved DOC from the NNet was evaluated by the MAPD between observed and modeled DOC. The NNet model predicted DOC quite well (MAPD = 7.2%) when compared to available data with the great majority of errors within less than 10 μmol L^{-1} C (Figures 3 and 4 and Table S1). Bias in the neural network model will result in higher errors at very high DOC (within estuaries) and at very low DOC (offshore), which are areas beyond our MAB study region. The neural net model was then combined with outputs from a physical circulation model (see section 2.6) to obtain the DOC profiles at each month and grid cell, which is referred to as $\mathrm{DOC}_{\mathrm{NNet}}(x, y, z, t)$. The profiles were then normalized by the surface DOC value and estimated from the near-surface satellite DOC, $\mathrm{DOC}_{\mathrm{Sat}}(x, y, t)$, as follows:

$$\mathrm{DOC}(x,y,z,t)=\mathrm{DOC}_{\mathrm{NNet}}(x,y,z,t)\times\frac{\mathrm{DOC}_{\mathrm{Sat}}(x,y,t)}{\mathrm{DOC}^{\mathrm{Max}}_{\mathrm{NNet}}(x,y,t)} \quad (6)$$

2.6. Integrated Tracer Flux Using Satellite-Derived DOC and Ocean Model Products

To describe ocean physical parameters (*T*, *S*, and velocity components), we used output from the Regional Ocean Modeling System (ROMS) Experimental System for Predicting Shelf and Slope Optics (ESPreSSO) model, which covers the MAB from the center of Cape Cod southward to the south of Cape Hatteras, from the shore to beyond the shelf break and shelf/slope front (Figure 5). The ESPreSSO system uses Four-Dimensional Variational data assimilation [*Zhang et al.*, 2010; *Zavala-Garay et al.*, 2012] to merge dynamic and kinematic constraints embodied in the ROMS hydrodynamic kernel with hourly surface velocity observations from high-frequency radar, sea surface temperature from Advanced Very High Resolution Radiometer passes and multiplatform optimally interpolated blended products, along-track altimeter sea level data from the Radar Altimeter Database System, and available in situ temperature and salinity data. The resulting data-constrained model-based analyses of ocean physical parameters have the highest (~5 km) horizontal resolution currently available for the region among such products. In an assessment of seven real-time models of MAB 3-D circulation for the period 2010–2011, no model was more skillful than ESPreSSO [*Wilkin and Hunter*, 2013], and ESPreSSO analyses have underpinned several applied studies of the MAB related to ecosystems [*Hu et al.*, 2012] and sediment transport [*Dalyander et al.*, 2013].

Using 3-D velocity from ESPreSSO, the elemental lateral DOC tracer flux is computed using the following equations:

$$Fx=\mathrm{DOC}(x,y,z,t)\times u(x,y,z,t)\times\Delta y\times\Delta z \quad (7)$$

$$Fy=\mathrm{DOC}(x,y,z,t)\times v(x,y,z,t)\times\Delta x\times\Delta z \quad (8)$$

where DOC is the monthly four-dimensional satellite-derived DOC concentration from equation (6), *u* and *v* are the monthly averaged four-dimensional ESPreSSO velocity components, and Δx, Δy, and Δz are the model grid cell dimensions.

We then calculate the vertically integrated DOC tracer flux at each horizontal grid cell of the MAB's open boundaries, which are in the southwest (SW), the northeast (NE), and along the 100 m isobaths at cross-shelf (CS) locations (Figure 5). Finally, the total annual integrated flux was obtained by adding the contributions of each boundary cell along each of the three open boundaries and estuary mouths. For control purposes, we also estimated the integrated volume transports at each of the shelf open boundaries and then computed the net flow balance. The balance was not perfect due to numerical uncertainties in calculating the volume transport along the boundaries, especially along the extensive cross-shelf boundary

(100 m isobath), but the imbalance was on average less than 5%. To make the net flow balance equal zero, we applied weighted averaged correction coefficients proportional to the volume transport at each individual boundary. After correction, the mean volume transports (in sverdrups, Sv, or 10^6 m^3 s^{-1}) for 2010–2012 were 0.47 Sv for the SW boundary, 0.60 Sv for the NE boundary, and −1.09 Sv for the CS boundary (positive and negative values indicate flow into and out of the MAB, respectively). The total transport from estuaries to the MAB for the same period was 0.017 Sv.

We applied the integrated DOC tracer flux approach to estimate the DOC export at the mouths of all MAB estuaries represented in ESPreSSO using equations (6)–(8), similar to the approach used for the three open shelf boundaries. The estuarine flux was computed using regional DOC algorithms determined from the three major estuarine outflows. The DOC algorithms from the Hudson-Raritan Estuary, Delaware Bay, and Chesapeake Bay were applied for the river or estuary outflows north of 39°N, between 39° and 38°N, and south of 38°N, respectively.

The uncertainty on the DOC flux is calculated using the bootstrap method based on the MATLAB function “bootci.” To estimate the 95% confidence interval (CI) on the shelf boundary DOC fluxes, we applied bootstrap resampling with replacement to the satellite versus NNet DOC percent differences (errors) for each of the boundaries to create 10,000 data sets of the errors. A probability distribution of the error was then constructed and estimates of the error (in percent) were calculated at the 2.5 and 97.5 percentiles of the corresponding probability distributions. Upper and lower bound estimates of the DOC flux were then calculated based on the error bound analysis for DOC concentrations at the 95% CI. The error on the ESPreSSO volume transport is unknown and was therefore not accounted for in this study. We also accounted for the uncertainty in DOC profiles by applying the quadrature sum of squares approach for the computed MAPDs of the DOC satellite algorithm and the vertical DOC profiles from the NNet model. The DOC concentration uncertainty would be equal to the square root of the summed squared MAPDs from the MODIS DOC retrievals (13.9%; section 3.2) and the NNet DOC profiles (7.2%; section 2.5), 15.7%. The total DOC flux uncertainties (95% confidence intervals) determined by the bootstrap method and presented in subsequent sections account for the error between the NNet DOC profiles and satellite DOC.

3. Results

3.1. Relationships of DOC to CDOM Optical Properties

DOC was strongly correlated to CDOM optical properties across a wide spectral range from the ultraviolet to blue wavelengths within the MAB, GoMa, and across the bay mouths (lower bay to plumes) of the MAB estuaries studied, which include the lower bay areas of Chesapeake Bay, Delaware Bay, and Hudson-Raritan Estuary (Figures 6, 7, and S2). As observed previously for the middle and southern MAB [*Mannino et al.*, 2008], the strong linear relationships between DOC and a_{CDOM} varied across seasons, regions (GoMa, northern MAB, and southern MAB), and estuaries due to different source contributions and loss processes for both CDOM and DOC. Two distinct seasonal DOC-to-a_{CDOM} relationships were observed for each subregion and region spanning from autumn to late

spring (designated fall-winter-spring or FWS; Figures 6a and 6e) and late spring to end of summer (designated summer; Figures 6b and 6f). The amount of DOC per unit a_{CDOM} increases from FWS to summer across the entire study region (Figure 6). A spatial pattern also emerged from these data. The amount of DOC per unit a_{CDOM} increases from the Gulf of Maine to the southern MAB (Figure 6c). The measurements from the MAB were merged to derive two seasonally based equations relating DOC to $a_{CDOM}(412)$ (Figure 6d). The survey cruise data used to validate the DOC algorithm and DOC-to-a_{CDOM} correlations (cruises notated as CV) demonstrate that these equations are consistent from year to year across the entire MAB region (Figure 6d). The extensive data set from the lower Chesapeake Bay and plume region spanning from July 2004 to August 2007 demonstrated strong consistency of the seasonal DOC-to-a_{CDOM} relationships (Figures 6e and 6f). While the y intercepts for the Chesapeake Bay data were similar for both seasons and with the MAB-wide FWS relationship, the slopes were quite different from each other (231 μmol L^{-1} m^{-1} for FWS and 300 μmol L^{-1} m^{-1} for summer) compared to the MAB slopes, which were similar (224 and 229 μM m^{-1} for FWS and summer, respectively). The FWS measurements yielded a better linear fit than the summer data in all regions studied. The GoMa relationships from the 2007 samples collected in the western Gulf of Maine were quite strong (Figures 6a and 6c), but the CV cruise data collected throughout the Gulf of Maine in summer do not yield a strong summer relationship ($y = 135x + 67.8$; $R^2 = 0.45$; data not shown). Also, several samples from the CV FWS cruises do not follow the 2007 relationships ($y = 113x + 62.9$; $R^2 = 0.33$; data not shown).

Several factors are believed to contribute to the strong linear DOC-to-a_{CDOM} relationships, especially for the FWS period. Generally, both DOC and a_{CDOM} decrease with depth, and this occurs in approximately linear manner during FWS but not during summer. For the FWS relationships, the profile DOC and a_{CDOM} data from the top ~100 m were applied to develop the DOC-to-a_{CDOM} relationships. The water column was generally not stratified (or weakly stratified) during the FWS period except within estuarine plumes where a two-layer circulation generally prevailed. Thus, the estuarine plume to offshore horizontal and vertical gradients can be characterized conceptually as the mixing of two pools of DOM, estuarine (high DOC and a_{CDOM}), and oceanic (low DOC and a_{CDOM}). For the summer period when the water column is strongly stratified, only the surface mixed-layer observations were applied to compute the DOC-to-a_{CDOM} linear relationships. During this period, river discharge is generally lowest in the watersheds that drain into the MAB resulting in lower CDOM and DOC within the estuarine plumes. In addition, marine production elevates DOC concentrations on the MAB shelf (primarily noncolored DOM), while photooxidation reduces a_{CDOM} levels. Thus, the DOC-to-a_{CDOM} ratio within surface waters increases during summer with respect to FWS. Under stratified conditions, photooxidation would primarily impact the surface mixed-layer DOM, whereas during the FWS period, photooxidation-induced changes to DOM would be assimilated throughout the water column with the exception of the plume regions where the water column is typically stratified. These circumstances alter the character of the DOM within and below the surface mixed layer during summer, resulting in a decrease in the DOC-to-a_{CDOM} ratio at depth while the ratio increases in the surface layer.

Another approach was investigated to obtain DOC from CDOM optical properties to avoid the need for multiple seasonal and regional DOC-to-a_{CDOM} relationships. Following a similar formulation to *Fichot and Benner* [2012], we obtained DOC through nonlinear regression curve fitting of the specific CDOM absorption coefficient (a_{CDOM}*(380) = a_{CDOM}(380)/DOC; with DOC in mg L^{-1}) against CDOM spectral slope for the 275 to 295 nm wavelength range ($S_{275–295}$). $S_{275–295}$ is derived from a fit of $a_{CDOM}(\lambda)$ between λ = 275 and 295 nm using the following equation:

$$a_{\mathrm{CDOM}}(\lambda)=a_{\mathrm{CDOM}}(\lambda_o) \times exp[S_{275-295}(l-\lambda_o)] \quad (9)$$

where λ_o represents the reference wavelength (275 nm in this case). Both power and exponential functions fit the MAB and GoMa data quite well (low RMSE and $R^2 > 0.96$; Figure 7 and Table 1). The nonlinear model fits for each region and for both regions combined were almost indistinguishable when plotted together for various specific CDOM absorption wavelengths including a_{CDOM}*(380), a_{CDOM}*(412), and a_{CDOM}*(355) (plot not shown). To evaluate whether these models would be appropriate for retrieving DOC, we computed DOC from these models with inputs of field measurements of $S_{275–295}$ and a_{CDOM}(380), a_{CDOM}(412), or a_{CDOM}(355). DOC retrieved from the nonlinear models matched the measured DOC (Figure 8). From the field data evaluation, the nonlinear approach retrieved DOC as well as the linear a_{CDOM}-to-DOC approach (Figure 8a). Furthermore, the nonlinear exponential equation developed by *Fichot and Benner* [2012] for the northern Gulf of Mexico was applied to our MAB and GoMa field data to demonstrate whether this approach would be transferrable to the MAB and GoMa. Our results show that the northern Gulf of Mexico equation retrieves DOC almost as well as the equation derived with our in situ data (Figure 8d). Separate sets of seasonal algorithms were determined for each lower estuary-plume region studied (Table 2). Since the nonlinear power and exponential models for the MAB region only and for both MAB and GoMa regions yielded nearly identical results, only the algorithms derived from the combined MAB and GoMa data sets are presented and discussed.

3.2. DOC Algorithm Validation

The in situ bio-optical DOC algorithms were applied to SeaWiFS and MODIS Aqua retrievals of $a_{CDOM}(\lambda)$ and $S_{275–295}$ [*Mannino et al.*, 2014] in order to create satellite-based estimates of DOC, which were then evaluated using validation matchups. The estuary-plume DOC algorithms shown in Table 2 could not be independently validated due to an insufficient number of satellite and in situ matchups. For the MAB algorithms, the MAPD of the matchup data ranged from 11.1 ± 7.5% for the linear a_{CDOM}(412) algorithm with SeaWiFS to 18.8 ± 11.4% for the exponential a_{CDOM}(355) algorithm with MODIS (Table 3). The other statistical results and the one-to-one plots of in situ DOC versus satellite DOC also indicated that the linear a_{CDOM}(412) algorithm was the better algorithm for retrieval of DOC from MODIS and SeaWiFS (Figure 9 and Table 3). Hence, the linear a_{CDOM} (412) algorithms were used to compute satellite DOC for the MAB region and individual estuaries and the two following time periods: 16 June to 30 September (summer) and 1 November to 15 May (FWS; Table 2). For the interleaving periods of 16 May to 15 June and 1–31

October a linear interpolation was derived to proportionally blend the two algorithms for those periods.

3.3. DOC Distributions and Integrated DOC Stocks

A 7 year (2006–2012) monthly climatology of MODIS Aqua DOC distributions was processed for the MAB to examine seasonal and spatial variability in DOC concentrations. The satellite climatology shows considerable month-to-month variability in DOC concentrations (Figure 10). DOC concentrations peaked in early spring and late summer (August–September) and expressed minima in May and November–December. The DOC climatology was consistent with the expected DOC gradient of decreasing DOC from the coast to the edge of the continental margin. The satellite images for March and September 2011 showed considerably higher DOC compared to the climatology distributions for those months, while DOC concentrations were similar for the months when DOC was lowest in 2011 (January and May) and the DOC climatology (November–December and May) (Figure 10). However, DOC in January 2011 was noticeably lower than observed in the January climatology. Such findings illustrate that DOC distributions in the MAB experience some level of interannual variability.

For the 2010–2012 period analyzed, the volume-averaged DOC concentration was 105.7 μmol L^{-1} on the inner shelf (0–25 m bottom depth), 84.3 μM on the midshelf (25–60 m), and 73.1 μmol L^{-1} on the outer shelf (60–100 m). The mean volume-averaged DOC concentrations for all combined estuaries and the SW, NE, and CS boundaries were 111.9, 70.7, 90.1, and 70.0 μmol L^{-1}, respectively (Table 4). The estuarine DOC value of 111.9 μmol L^{-1} was within 7% of the equivalent value of 119.9 μmol L^{-1} calculated from the available observations within the mouths of Chesapeake Bay, Delaware Bay [*Sharp et al.*, 2009] (J. Sharp, unpublished data, 2014; this study), and Hudson-Raritan Estuary.

Monthly time series of volume-integrated DOC stocks for the inner shelf, midshelf, outer shelf, and entire shelf are shown in Figure 11. The shelf volumes and 2010–2012 volume-integrated mean DOC stocks for the inner, middle, and outer shelves were 49.2 $\times 10^{10}$ m^3 and 0.62 ± 0.05 Tg C (± standard deviation of monthly values), 231 × 10^{10} m^3 and 2.3 ± 0.19 Tg C, and 226 × 10^{10} m^3 and 2.0 ± 0.17 Tg C, respectively. The equivalent values for the entire MAB shelf (to 100 m depth) were 506 × 10^{10} m^3 and 4.9 ± 0.4 Tg C. The two distinct peaks appearing on the record in all regions, one in the spring and one in the fall, were most likely a result of higher net DOC production on the shelf during those months (Figure 11). During 2011, there was a 59–80% increase of the amplitude in the annual cycle (defined as the maximum minus the minimum) of DOC stocks from 0.9 and 1 Tg C in 2010 and 2012, respectively, to 1.5 Tg C in 2011 across the continental shelf.

3.4. Estuarine DOC Concentrations and Export

We applied regional DOC algorithms (Table 2) to estimate estuarine DOC concentrations and the total estuarine export of DOC (Table 2). The mean surface layer DOC concentrations at the mouths of Chesapeake Bay (125 μmol L^{-1} C) and Delaware Bay (128 μmol L^{-1} C) were very similar, while the value at the Hudson-Raritan Estuary mouth was about 15% lower (107 μmol L^{-1} C). The 2010–2012 monthly time series of estuarine DOC fluxes at the

mouths of the three major estuaries combined was 0.63 Tg C yr^{-1}, or 81% of the total (0.77 Tg C yr^{-1}) for all the MAB estuaries (Figure 12b). For comparison, we calculated the total estuarine DOC export based on the mean DOC concentrations at the mouths of the three estuaries from Table 4 (119.9 μmol L^{-1} C) and the 3 year mean total estuarine volume transport from ESPreSSO (0.017 Sv), which equals 0.77 Tg C yr^{-1}, exactly the same as the DOC export calculated using the integrated tracer transport method (Figure 12b and Table 5). Another approach applied to estimate estuarine DOC fluxes was based on the knowledge of the freshwater end-member ("zero" salinity) DOC concentration by extrapolating DOC and salinity from the lower bay and plume region to a hypothetical freshwater end-member (to obtain the "apparent" DOC end-member) as described by *Vlahos et al.* [2002] and the annual freshwater discharge to the MAB or a particular estuary mouth. This approach accounts for nonconservative mixing of DOC (production, consumption, and transformation) from the river mouth to the estuary mouth. Applying a 3 year mean freshwater discharge at the CB mouth from the United States Geological Survey (USGS) (Figure 12a; 2414 m^3 s^{-1}) or the MAB freshwater estuarine flux of 0.005 Sv from *Beardsley and Boicourt* [1981] and an apparent DOC end-member of 314.1 μM C for Chesapeake Bay based on our field measurements, the estimates for Chesapeake Bay and total MAB estuarine fluxes are 0.29 and 0.60 Tg C yr^{-1}, respectively, which yield similar values to our combined satellite and ESPreSSO modeling approach of 0.29 and 0.77 Tg C yr^{-1}, respectively. These estimates of DOC export are also consistent with other estimates from the recent literature. DOC export computed from a coupled biogeochemical-hydrodynamic model of the Chesapeake using C:N ratios of 12 (18) μM C:μM N for semilabile (refractory) DON, respectively, generated an average DOC export from 2001 to 2005 of 0.42 Tg C yr^{-1} [*Feng et al.*, 2015]; however, interannual variation was high, with values ranging from 0.22 Tg C yr^{-1} in the driest year (2002) to 0.66 Tg C yr^{-1}in the wettest year (2003). Our MAB estimates are also not statistically different from the MAB estuarine export of 1.0 (0.5, 1.3; 95% confidence intervals) Tg C yr^{-1} derived from a combination of total organic carbon (TOC) estuarine export given by *Herrmann et al.* [2015] using a steady state balance approach and an estuarine DOC/TOC ratio of 0.71 computed from our in situ data near the mouths of Chesapeake Bay, Delaware Bay, and Hudson-Raritan Estuary [*Sharp et al.*, 2009; K. C. Filippino, unpublished data, 2012; A. Mannino, unpublished data, 2014; J. Sharp, unpublished data, 2014].

3.5. DOC Fluxes Along the Shelf Open Boundaries

The DOC fluxes along the open boundaries of the MAB shelf were highly dynamic temporally, from month to month and year to year, as well as spatially. Along the NE and SW boundaries, the DOC fluxes were on average directed into the MAB for all months within the 3 year time series (positive values). In contrast, the CS fluxes were directed out of the MAB shelf (negative values) with only five months from 2010 to 2012 showing net inputs of DOC to the shelf from offshore (October 2010, February and December 2011, and January and September 2012; positive values) (Figure 12c). The monthly DOC fluxes expressed minima and maxima (in absolute terms) ranging from 6.7 to 37.5 Tg C yr^{-1} (NE), 2.5 to 25.7 Tg C yr^{-1} (SW), and 84.8 to 30.4 Tg C yr^{-1} (CS). A few seasonal patterns were revealed. The SW DOC fluxes peaked in summer with minima in late fall-winter. In contrast, the NE fluxes peaked in October–December of each year, but no other seasonal

patterns were observed. One consistent pattern observed for the CS boundary was the high offshore CS flux in March of each year. The annual mean DOC fluxes were similar from year to year for the SW (11.2 to 13.9 Tg C yr^{-1}) but much more variable for the NE (14.1 to 23.6 Tg C yr^{-1}) and the CS (−24.6 to 32.9 Tg C yr^{-1}) boundaries (Table 5).

To investigate the spatial variability of DOC fluxes, the CS boundary was subdivided into five regional segments. The most southern segment (34.5° to 35.5°N) was subdivided into three shorter sections (Figure 5). On average, DOC flowed into the MAB along the two most southern sections of the CS boundary, which are on the western side of the Gulf Stream, whereas for the other four segments and the section to the east of Cape Hatteras, DOC flowed out of the MAB. The two segments to the north (35.5° to 39°N) demonstrated the greatest offshore flux of DOC with the boundary off the coast of Chesapeake Bay yielding a DOC flux of −14.6 Tg C yr^{-1} and −8.7 Tg C yr^{-1} for the boundary offshore of Delaware Bay (Figure 5b).

3.6. MAB DOC Budget

A DOC budget for the MAB was constructed with the monthly changes in DOC stocks and lateral DOC fluxes and literature values of other inputs and losses of DOC (Figure 13). The net community production (NCP) of DOC in the MAB was computed monthly as the difference of inputs and losses of DOC using the following equations:

$$\text{NCP of DOC} = (\text{DOC losses} - \text{DOC inputs}) + \text{change in DOC stocks} \quad (10)$$

$$\text{DOC losses} = \text{CS fluxes out of the MAB} + \text{photooxidation} \quad (11)$$

$$\text{DOC inputs} = \text{Estuaries} + \text{NE} + \text{SW} + \text{CS fluxes into MAB} + \text{sediments} + \text{rainfall} \quad (12)$$

Our estimate for NCP of DOC is −2.6 ± 0.89 Tg C yr^{-1} (3 year mean ± standard deviation of three annual values; Figure 13).

4. Discussion

4.1. DOC Algorithm and Distributions

Algorithms for satellite retrieval of DOC from CDOM optical properties were developed from field measurements and validated with MODIS and SeaWiFS reflectances to obtain stocks and fluxes of DOC within our study region. The linear algorithms that relate DOC to $a_{CDOM}(412)$ on a seasonal and regional basis provided MODIS Aqua and SeaWiFS DOC values closer in agreement with the field measurements than the power law or exponential algorithms, which would have been appropriate across all seasons and study areas. The combined errors in the satellite $S_{275–295}$ and $a_{CDOM}(\lambda)$ products, which are due to errors in satellite remote sensing reflectances, yielded the poorer validation results for the power law

and exponential DOC algorithms. Several factors including inadequate atmospheric correction contributed to the uncertainties in MODIS and SeaWiFS remote sensing reflectances and CDOM properties within our study region [*Mannino et al.*, 2014]. Linear relationships of DOC with a_{CDOM} at other wavelengths from <300 nm to 450 nm would have yielded similarly good relationships (Figure S2) based on the strong correlations between DOC and a_{CDOM} at these other wavelengths and equivalent validation results of satellite a_{CDOM} at these other wavelengths from SeaWiFS and MODIS reflectances [*Mannino et al.*, 2014]. Prior studies on satellite retrievals of DOC have involved the utilization of linear relationships between DOC and (1) $a_{CDOM}(412)$ [*Del Castillo and Miller*, 2008], (2) $a_{CDOM}(443)$ [*Matsuoka et al.*, 2013], (3) $a_{CDOM}(355)$ [*Mannino et al.*, 2008; *Liu et al.*, 2014], (4) $a_{CDOM}(400)$ [*Griffin et al.*, 2011], (5) salinity computed from $a_{CDOM}(443)$ [*López et al.*, 2012], (6) chlorophyll *a* and $a_{CDOM}(355)$ [*Liu et al.*, 2014], (7) salinity and $a_{CDOM}(355)$ (D. A. Aurin et al., Remote Sensing of CDOM and Dissolved Organic Carbon in the Global Ocean, *Remote Sensing Environment*, manuscript in revision, 2015), and (8) also a neural network algorithm that employed remote sensing reflectances as model inputs [*Korosov et al.*, 2012]. To our knowledge, the only satellite-derived DOC distributions that have been formally validated with coincident (±3 h) satellite and in situ matchup data were accomplished by *Mannino et al.* [2008], Aurin et al. (manuscript in revision, 2015), and the work described herein. DOC concentrations in the MAB were highest in the vicinity of the estuary mouths, along the shoreline, and southeast of Cape Cod and lowest offshore and to the southeast as shown in the monthly satellite derived DOC climatology (Figure 10). The seasonal trends in satellite surface DOC and water-column-integrated DOC stocks were consistent with higher estuarine export, alongshore inputs from the NE and SW boundaries, and net community production (NCP) of DOC on the shelf from late winter to early spring followed by a decline in DOC through spring from reduced inputs (Figures 10 and 11). Through summer, DOC on the shelf increased presumably on account of higher NCP. The increase in DOC stocks from May to September ranged from 19% in 2010 to 35% in 2012. The seasonal increase of DOC concentrations from spring to late summer in the MAB was previously observed in field data collected in 1996 [*Vlahos et al.*, 2002] and both field measurements and satellite data from 2005 to 2006 [*Mannino et al.*, 2008]. From early fall to early winter, satellite DOC concentrations and DOC stocks decreased, which can be attributed to microbial decomposition of DOC produced during summer.

4.2. Evaluation of Model Water Volume Transport

The volume transports from the ESPreSSO model applied in this study have not been previously evaluated due to insufficient field observations. However, the model has been shown to capture the circulation and dynamics of the MAB [*Dalyander et al.*, 2013; *Wilkin and Hunter*, 2013]. Furthermore, comparisons of ESPreSSO model results of temperature and salinity profiles and surface currents with field observations has demonstrated that ESPreSSO performs very well in reproducing these parameters [*Wilkin and Hunter*, 2013]. Our application of the ESPreSSO model depended primarily on the temperature and salinity profiles for computing DOC stocks and the velocity vectors along the MAB study domain boundaries to compute fluxes. Because of the model's horizontal resolution, there was greater uncertainty on how well it simulated the circulation within estuaries and the

boundaries between the estuaries and coastal ocean. Given that any uncertainty in volume transports will affect the computed DOC fluxes, a compilation of volume transport values determined from field-based observations within the study region was provided for comparisons with ESPreSSO results (Table 6 and Figure 5a). The estuarine water volume transports from ESPreSSO were in reasonable agreement with field observations. The southward alongshore water flux along the northeast boundary has been estimated at 0.4 to 0.64 Sv, which compares well with the ESPreSSO value of 0.60 Sv [e.g., *Fratantoni et al.*, 2001] (Table 6). The greatest discrepancy in volume transport was found at the SW boundary, where the northward alongshore flow from ESPreSSO (0.48 Sv) was substantially larger than field observations (0.1 to 0.24 Sv) [*Flagg*, 1977; *Beardsley and Boicourt*, 1981; *Savidge and Bane*, 2001]. This can be attributed to the more southern location of the SW boundary (just north of Cape Lookout) than field observations (near Cape Hatteras) as well as the complex circulation dynamics within the southern MAB and northern South Atlantic Bight (SAB) [*Savidge and Bane*, 2001; *Churchill and Gawarkiewicz*, 2012; *Savidge and Savidge*, 2014]. The net cross-shelf water volume transport for the entire MAB boundary from ESPreSSO (−1.09 Sv) was similar to the range of values from the observational literature (−0.14 to −1.3 Sv), which includes export through filaments (−0.1 to −0.9 Sv) [*Lillibridge et al.*, 1990; *Joyce et al.*, 1992] and eddies (−0.13 Sv) [*Churchill et al.*, 1993] (Table 6 and Figure 5a). Along the southernmost cross-shelf segment (34.5° to 35.5°N), the net cross-shelf transports were shoreward (positive) on average for the two southern sections of the segment, ranging from 0.007 to 0.343 Sv for the northernmost to southernmost sections, respectively. Within the SAB and the southern segment of our study region, the Gulf Stream interacts directly with the continental shelf, which permits Gulf Stream waters to intrude onto the shelf primarily during winter [*Verity et al.*, 1993]. Shoreward cross-shelf transport along this CS segment has been observed in the field but not quantified [*Churchill and Cornillon*, 1991; *Churchill and Berger*, 1998; *Savidge*, 2002].

The ESPreSSO model seems to capture some aspects of the complex dynamics where MAB and SAB waters meet. The southward flowing MAB shelf waters and northward flowing SAB shelf waters converge near Cape Hatteras and form the Hatteras Front, which is in the vicinity of where the Gulf Stream shears away from the shelf toward the northeast [*Churchill and Berger*, 1998; *Savidge and Bane*, 2001]. This convergence forces MAB (and SAB) shelf water to flow offshore (to the northeast) [*Churchill and Gawarkiewicz*, 2012]. Summer maxima in ESPreSSO SW water volume transport were consistent with field observations that show a northward flow into the MAB [*Savidge and Bane*, 2001; *Savidge and Savidge*, 2014]. The CS export flux near Cape Hatteras likely includes the export of SAB shelf water in addition to MAB shelf water in approximately equal proportions with a maximum amount of SAB shelf water export occurring during summer [*Savidge and Savidge*, 2014]. The cross-shelf transport of water onto the shelf from offshore for the region south of Cape Hatteras found in ESPreSSO (Figure 5a) has been observed along the Hatteras Front during fall and winter [*Savidge*, 2002; *Savidge et al.*, 2012].

4.3. DOC Fluxes and Budget

The 3 year time series of DOC stocks and fluxes demonstrate substantial interannual variability. Very high levels of precipitation fell within MAB watersheds in 2011, yielding

above-normal freshwater discharge by rivers to the MAB. The greater amplitude of DOC stocks in 2011 compared to 2010 or 2012 was consistent with greater (approximately double) river discharge to the MAB and presumably commensurately higher dissolved inorganic nitrogen export during that year, which could have resulted in higher primary productivity in the estuaries and shelf waters of the MAB and thus higher DOC stocks. The dissolved inorganic nitrogen entering Chesapeake Bay from rivers, wastewater, nonpoint sources, and atmospheric deposition was 0.23 Tg N yr^{-1} in 2011 compared to 0.13 and 0.12 Tg N yr^{-1} for 2010 and 2012, respectively (Chesapeake Bay Program; http://www.chesapeakebay.net/indicators/indicator/nitrogen_loads_and_river_flow_to_the_bay1) These findings are consistent with our time series of the Chesapeake Bay DOC flux at the mouth of the bay calculated in this study, combined with the United States Geological Survey (USGS; http://md.water.usgs.gov/waterdata/chesinflow/) freshwater discharge at the same approximate transect location as well as the Susquehanna River freshwater discharge (Figure 12a). There was a correlation between high DOC flux and peak freshwater discharge, as well as higher mean annual DOC flux and freshwater discharge in 2011. The freshwater discharge at the mouth of Chesapeake Bay for years 2010, 2011, and 2012 was 2146, 3541, and 1797 $m^3\ s^{-1}$, respectively. The corresponding values for the Susquehanna River were 1029, 2080, and 880 $m^3\ s^{-1}$, which account for roughly half of the river discharge entering the Bay. The DOC export fluxes at the mouth of Chesapeake Bay for the three years were 0.29, 0.34, and 0.24 Tg C yr^{-1}, which correspond to the interannual fluctuations in freshwater discharge. Similarly, large interannual variability in freshwater discharge and dissolved organic matter export has been reported using a biogeochemical-hydrodynamic model of the Chesapeake Bay [*Feng et al.*, 2015]. Over the years 2001–2005, freshwater discharge averaged 2681 $m^3\ s^{-1}$, but in the high flow year of 2003 that was associated with Hurricane Isabel, average freshwater discharge reached 4605 $m^3\ s^{-1}$. Over these five years DOC export averaged 0.42 Tg C yr^{-1} but reached an average of 0.66 Tg C yr^{-1} in 2003 [*Feng et al.*, 2015], again demonstrating that DOC export at the mouth of the Chesapeake Bay is closely linked to interannual variations in freshwater discharge.

The shelf fluxes of DOC derived from our satellite and modeling approach were generally higher than prior estimates. Using field measurements of DOC from three cruises between 1994 and 1996 and literature values of water transport along the MAB boundaries, *Vlahos et al.* [2002] estimated DOC inputs to the shelf from the NE at 10.6 to 11.4 Tg C yr^{-1} and 1.9 Tg C yr^{-1} from the Gulf Stream and cross-shelf DOC export of −18.7 to −19.6 Tg C yr^{-1}, which included the export of shelf DOC through Gulf Stream entrainment of shelf water within filaments and displacement of shelf water by Gulf Stream eddies that move onto the shelf in the vicinity of and north of Cape Hatteras (−8.4 Tg C yr^{-1}; see Table 6 for volume transport). *Bates and Hansell* [1999] estimated cross-shelf fluxes of −2.7 and −31 Tg C yr^{-1} solely within fast flowing filaments off the coast of Cape Hatteras that flow along the western edge of the Gulf Stream [*Ford et al.*, 1952; *Biscaye et al.*, 1994]. They applied DOC from a late September to early October 1996 cruise between Chesapeake Bay and Bermuda and shelf water fluxes of 0.13 Sv [*Churchill et al.*, 1993] and 1.5 Sv [*Walsh*, 1994], respectively. The locations of these filaments corresponded to the southern portion (~35.5 to 36.5°N) of the cross-shelf segment with the highest DOC flux and water volume transport of our study region (Figure 5). The higher DOC fluxes obtained from our approach using

MODIS-derived DOC and models (NE = 18.6 Tg C yr^{-1}, SW = 12.1 Tg C yr^{-1}, and CS = −29 Tg C yr^{-1}) were attributed primarily to the higher volume transports from the ESPreSSO model compared to the values applied by *Vlahos et al.* [2002] (50% higher for NE; 2.2 times higher along CS boundary). The higher volume transports produced by ESPreSSO were corroborated with estimates of volume transports obtained from field observations (Table 6).

The cross-shelf DOC fluxes were considerably more dynamic temporally (3 times greater amplitude) and spatially than along-shelf fluxes (Figures 5b and 12c) affirming that physical processes drive the magnitude of cross-shelf fluxes of DOC as opposed to DOC concentrations. The intra-annual range of cross-shelf fluxes was substantial ranging from 30.4 Tg C yr^{-1} in October 2010 (net flux into the shelf) to −84.8 Tg C yr^{-1} in March 2010. The high CS fluxes of DOC offshore between 35.5° and 39°N were consistent with field observations of high water volume transport along this region in part due to the presence of filaments and eddies and consistent with the assertions of *Bates and Hansell* [1999]. The CS fluxes along the segment between 35.5° and 37.5°N varied significantly from year to year (−14, −10.4, and −19.4 Tg C yr^{-1} for 2010–2012). The most southern segment, 34.5° to 35.5°N, ranged from −3.1 to +3.1 Tg C yr^{-1} between 2010 and 2012 revealing cross-shelf DOC flowing in opposite directions across this boundary.

The alongshore and CS fluxes were significantly greater in magnitude than DOC stocks or in situ production supporting the premise that coastal circulation processes regulate the large-scale distributions of DOC on the shelf. From an estimated MAB primary production rate of 34 Tg C yr^{-1} [*Najjar et al.*, 2012], DOC released directly by phytoplankton contributes ~6 Tg C yr^{-1} (assumes an extracellular DOC release of 17.5%) [*O'Reilly et al.*, 1987] to the shelf, with the total contribution of primary production to the DOC pool through direct and indirect processes (e.g., viral lysis and sloppy feeding) estimated to be ~17 Tg C yr^{-1} (assumes 50% of primary production enters the DOC pool). The exchange of DOC and other constituents across the boundaries of continental margins such as the MAB and other margins with similar or higher alongshore and cross-shelf volume transport occurs at high temporal frequency and should be studied at subseasonal to daily time scales.

ESPreSSO model results applied to compute DOC fluxes were strictly limited to the chosen boundaries for the MAB. For example, if the SW boundary were to be shifted northward, then the water transport, and thus, DOC flux along that boundary would likely be significantly lower than 12.1 Tg C yr^{-1} and potentially close to 0 if shifted near Cape Hatteras. The SW boundary of our study domain was located farther south than the traditional MAB-SAB boundary of Cape Hatteras because of the narrow shelf near Cape Hatteras resulting in fewer model pixels and also due to the complex circulation processes described previously. Thus, the more southerly location for our SW boundary resulted in significant DOC fluxes into the MAB along this boundary because it was located south of the MAB-SAB shelf water convergence zone (Hatteras Front) where northerly volume transport is higher. *Vlahos et al.* [2002] did not provide an estimate of the net DOC flux along their southern alongshore boundary, which was farther north (near Cape Hatteras) than the SW boundary specified in our study.

On average the NCP estimated from the DOC budget was negative indicating that the MAB was net heterotrophic, meaning that in situ DOC remineralization exceeded DOC production (Figure 13). This estimate is significantly lower than the NCP value of 4.1–7.4 Tg C yr^{-1} computed by *Vlahos et al.* [2002]. However, if the SW boundary were shifted closer to Cape Hatteras (northward), it would likely result in a low (or near zero) SW flux out of the MAB. Under these circumstances, NCP of DOC would be positive (net autotrophic) for the MAB. Assuming a net zero SW flux would yield an NCP of DOC of 9.5 ± 1.1 Tg C yr^{-1}, which is much closer to the estimate of *Vlahos et al.* [2002]. The month-to-month variability in NCP was quite high (±22.6 Tg C yr^{-1}) as revealed by the wide range in CS monthly fluxes (Figure S3).

The higher DOC fluxes from this study compared to prior work [*Vlahos et al.*, 2002] reveal an even more significant role of DOC in the regional and global carbon cycle. To place this in context with other coastal carbon fluxes, the annual CS flux of DOC is equivalent to nearly 14 times the MAB air-sea CO_2 flux (−2.1 Tg yr^{-1}) [*Signorini et al.*, 2013] and 11.6% of the global continental margin air-sea CO_2 flux [*Cai*, 2011]. The MAB may account for 8–19% of the global export of DOC to the open ocean based on our annual mean CS flux (29 Tg C yr^{-1}) and the global DOC flux estimated by *Bauer et al.* [2013]. The export of higher levels of DOC to the open ocean provides a greater source of nutrients and energy to the ocean's microbial food web than previously thought. Furthermore, the cross-shelf high-volume offshore transport from the southern MAB (east and northeast of Cape Hatteras) can serve as a conduit for rapidly transporting terrestrial, estuarine, and shelf DOC into the ocean's interior that may be more labile due to a shorter residence time on the shelf. The subsidy of carbon received by the open ocean from the MAB and other continental margins must be taken into account within regional, basin-scale, and global biogeochemical models.

5. Conclusions

1. The Neural networks feed forward model predicted DOC vertical profiles quite well (MAPD = 7.2%) when compared to available field data with the great majority of errors less than 10 μmol L^{-1} C. Bias in the neural network model would result in higher errors at very high DOC (within estuaries) and at very low DOC (offshore of the continental margin), which represent areas beyond our MAB study region.
2. Model resolution with grid cell dimensions of 1 to 2 km would be more preferable than the coarser resolution of the ESPreSSO model for computing fluxes from estuaries and nearshore boundaries. Nevertheless, the DOC fluxes from MAB estuaries were equivalent to prior estimates when taking uncertainties into account.
3. Dissolved organic carbon cycling and cross-shelf fluxes in the northeastern U.S. are influenced by large-scale physical processes operating at subseasonal to interannual time scales

4. The high DOC cross-shelf flux estimated for the region between Cape Hatteras and Chesapeake Bay confirmed the importance of this region in exporting substantial quantities of carbon to the open ocean.
5. Our more comprehensive estimates using satellite data and model products yielded higher shelf fluxes of DOC than prior estimates.
6. Seasonal and interannual variability in DOC stocks and fluxes are significant and that short duration measurements (snapshots from a few cruises or a single year of satellite data) as well as climatological means would be inadequate to represent the dynamics of DOC fluxes (and budget) of continental margins.
7. The approach of combining field measurements, satellite observations, and model results provided a comprehensive and presumably more robust assessment of shelf DOC fluxes and stocks. Satellite measurements and model results are essential for capturing the monthly, seasonal, and interannual variability observed in the MAB.
8. DOC advective fluxes are an important component of the carbon budget because the fluxes are larger or comparable to other terms, like the air-sea CO_2 flux and primary production.

Future work will extend the analysis to more recent years and include the computation of fluxes for particulate organic carbon following a similar approach as presented in this study. In addition, an increase in the numerical model resolution, primarily within the estuaries and their outflow areas, combined with the full satellite data resolution of 1 km, could potentially provide more accurate assessments of carbon fluxes.

Supplementary Material

Refer to Web version on PubMed Central for supplementary material.

Acknowledgments

We want to acknowledge the NASA Interdisciplinary Science Program (USECoS Project) and Ocean Biology and Biogeochemistry Program (CliVEC Project) for supporting this work. We thank the Editor and two anonymous reviewers for their comments, which helped us to improve this manuscript. Our sincere gratitude to Katherine Filippino, Mary Russ, Veronica Lance, Xiaoju Pan, and Dirk Aurin for assistance with sample collection. We are grateful to Jerry Prezioso, Jon Hare, and Harvey Walsh for accommodating our CliVEC project on NOAA's Northeast Marine Fisheries Service Ecosystem Monitoring (ECO-Mon) cruises and Tamara Holzwarth-Davis for processing the CTD profile data. We thank Mike Twardowski for organizing several cruises in the Hudson-Raritan Estuary and adjacent shelf and Ru Morrison for inviting us to participate on cruises in the Gulf of Maine. Thanks to Jay Austin, Eileen Hofmann, and John Klinck for planning or assistance with the Old Dominion University Chesapeake Bay mouth hydrography transects and data access. The USECoS team members provided many useful comments. We extend our profound appreciation to the Ocean Biology Processing Group (OBPG) at the NASA Goddard Space Flight Center for the distribution of and continuing efforts in improving MODIS and SeaWiFS data products. Measurements from the field sampling described in this manuscript were archived in the NASA SeaWiFS Bio-optical Archive and Storage System (http://seabass.gsfc.nasa.gov/).

References

Anderson R, Rowe G, Kemp P, Trumbore S, Biscaye P. Carbon budget for the mid-slope depocenter of the Middle Atlantic Bight. Deep Sea Res Part II. 1994; 41:669–703.

Bailey SW, Werdell PJ. A multi-sensor approach for the on-orbit validation of ocean color satellite data products. Remote Sens Environ. 2006; 102:12–23.

Bates NR, Hansell DA. A high resolution study of surface layer hydrographic and biogeochemical properties between Chesapeake Bay and Bermuda. Mar Chem. 1999; 67:1–16.

Bauer JE, Druffel ERM, Wolgast DM, Griffin S. Sources and cycling of dissolved and particulate organic radiocarbon in the Northwest Atlantic Continental Margin. Global Biogeochem Cycles. 2001; 15(3):615–636. DOI: 10.1029/2000GB001314

Bauer JE, Druffel ERM, Wolgast DM, Griffin S. Temporal and regional variability in sources and cycling of DOC and POC in the northwest Atlantic continental shelf and slope. Deep Sea Res, Part II. 2002; 49(20):4387–4419. DOI: 10.1016/s0967-0645(02)00123-6

Bauer JE, Cai W-J, Raymond PA, Bianchi TS, Hopkinson CS, Regnier PAG. The changing carbon cycle of the coastal ocean. Nature. 2013; 504:61–70. DOI: 10.1038/nature12857 [PubMed: 24305149]

Beardsley, RC., Boicourt, WC. On estuarine and continentalshelf circulation in the Middle Atlantic Bight. In: Warren, BA., Wunsch, C., editors. Evolution of Physical Oceanography, Scientific Surveys in Honor of Henry Stommel. MIT Press; Cambridge, Mass: 1981. p. 198-233.

Beardsley RC, Boicourt WC, Hansen DV. Physical oceanography of the Middle Atlantic Bight. Limnol Oceanogr. 1976; 2:20–34.

Benner R, Strom M. A critical evaluation of the analytical blank associated with DOC measurements by high-temperature catalytic oxidation. Mar Chem. 1993; 41:153–60.

Biscaye PE, Flagg CN, Falkowski PG. The shelf edge exchange processes experiment, SEEP-II: An introduction to hypotheses, results and conclusions. Deep Sea Res Part II. 1994; 41:231–252. DOI: 10.1016/0967-0645(94)90022-1

Blough, NV., Del Vecchio, R. Chromophoric DOM in the coastal environment. In: Hansell, DA., Carlson, CA., editors. Biogeochemistry of Marine Dissolved Organic Matter. Academic Press; San Diego, Calif: 2002. p. 509-546.

Brooks, DA. A brief overview of the physical oceanography of the Gulf of Maine. In: Wiggin, J., Moers, CNK., editors. Gulf of Maine Scientific Workshop. Gulf of Maine Council on the Marine Environment, Urban Harbors Institute, Univ of Massachusetts; Boston: 1992.

Cai WJ. Estuarine and coastal ocean carbon paradox: CO_2 sinks or sites of terrestrial carbon incineration? Annu Rev Mar Sci. 2011; 3:123–145.

Chapman DC, Beardsley RC. On the origin of shelf water in the Middle Atlantic Bight. J Phys Oceanogr. 1989; 19:384–391.

Chapman DC, Barth JA, Beardsley RC, Fairbanks RG. On the continuity of mean flow between the Scotian Shelf and the Middle Atlantic Bight. J Phys Oceanogr. 1986; 16:758–772.

Chen CTA, Wang S-L. Carbon, alkalinity and nutrient budgets on the East China Sea continental shelf. J Geophys Res. 1999; 104(C9):20,675–20,686. DOI: 10.1029/1999JC900055

Churchill JH, Berger TJ. Transport of Middle Atlantic Bight shelf water to the Gulf Stream near Cape Hatteras. J Geophys Res. 1998; 103(C13):30,605–30,621.

Churchill JH, Cornillon PC. Gulf Stream water on the shelf and upper slope north of Cape Hatteras. Cont Shelf Res. 1991; 11:409–431.

Churchill JH, Gawarkiewicz G. Shelfbreak frontal eddies over the continental slope north of Cape Hatteras. J Geophys Res. 2009; 114:C02017.doi: 10.1029/2007JC004642

Churchill JH, Gawarkiewicz GG. Pathways of shelf water export from the Hatteras shelf and slope. J Geophys Res. 2012; 117:C08023.doi: 10.1029/2012JC007995

Churchill JH, Levine ER, Connors DN, Cornillon PC. Mixing of shelf, slope and Gulf Stream water over the continental slope of the Middle Atlantic Bight. Deep Sea Res. 1993; 40:1063–1085.

Dalyander PS, Butman B, Sherwood CR, Signell RP, Wilkin JL. Characterizing wave- and current-induced bottom shear stress: U.S. middle Atlantic continental shelf. Cont Shelf Res. 2013; 52:73–86.

de Madron XD, et al. Nutrients and carbon budgets for the Gulf of Lion during the Moogli cruises. Oceanol Acta. 2003; 26:421–433.

Del Castillo CE, Miller RL. On the use of ocean color remote sensing to measure the transport of dissolved organic carbon by the Mississippi River Plume. Remote Sens Environ. 2008; 112:836–844.

Del Castillo CE, Coble PG, Morell JM, López JM, Corredor J. Analysis of the optical properties of the Orinoco River plume by absorption and fluorescence spectroscopy. Mar Chem. 1999; 66:35–51.

Del Vecchio R, Subramaniam A, Uz SS, Ballabrera-Poy J, Brown CW, Blough NV. Decadal time-series of SeaWiFS retrieved CDOM absorption and estimated CO_2 photoproduction on the continental shelf of the eastern United States. Geophys Res Lett. 2009; 36:L02602.doi: 10.1029/2008GL036169

Dong S, Kelly K. Seasonal and interannual variability in geostrophic velocity in the Middle Atlantic Bight. J Geophys Res. 2003; 108(C6):3172.doi: 10.1029/2002JC001357

Druon JN, Mannino A, Signorini S, McClain C, Friedrichs M, Wilkin J, Fennel K. Modeling the dynamics and export of dissolved organic matter in the northeastern U.S. continental shelf. Estuarine, Coastal Shelf Sci. 2010; 88:488–507.

Falkowski PG, Flagg CN, Rowe GT, Smith SL, Whitledge TE, Wirick CD. The fate of a spring diatom bloom: Export or oxidation? Cont Shelf Res. 1988; 8:457–484.

Falkowski PG, Biscaye PE, Sancetta C. The lateral flux of biogenic particles from the eastern North American continental margin to the North Atlantic Ocean. Deep Sea Res Part II. 1994; 41:583–601.

Feng Y, Friedrichs MAM, Wilkin J, Tian H, Yang Q, Hofmann EE, Wiggert JD, Hood RR. Chesapeake Bay nitrogen fluxes derived from a land-estuarine-ocean biogeochemical modeling system: Model description, evaluation and nitrogen budgets. J Geophys Res Biogeosci. 2015; 120:1666–1695. DOI: 10.1002/2015JG002931 [PubMed: 27668137]

Fennel K, Wilkin J, Previdi M, Najjar R. Denitrification effects on air-sea CO_2 flux in the coastal ocean: Simulations for the northwest North Atlantic. Geophys Res Lett. 2008; 35:L24608.doi: 10.1029/2008GL036147

Ferrari GM, Dowell MD, Grossi S, Targa C. Relationship between the optical properties of chromophoric dissolved organic matter and total concentrations of dissolved organic carbon in the southern Baltic Sea region. Mar Chem. 1996; 55:299–316.

Fichot CG, Benner R. A novel method to estimate DOC concentrations from CDOM absorption coefficients in coastal waters. Geophys Res Lett. 2011; 38:L03610.doi: 10.1029/2010GL046152

Fichot CG, Benner R. The spectral slope coefficient of chromophoric dissolved organic matter ($S_{275–295}$) as a tracer of terrigenous dissolved organic carbon in river-influenced ocean margins. Limnol Oceanogr. 2012; 57:1453–1466.

Flagg, CN. PhD thesis. Massachusetts Institute of Technology/Woods Hole Oceanographic Institution; 1977. The kinetics and dynamics of the New England continental shelf and the shelf/slope front; p. 207WHOI Ref. 77–67

Flagg CN, Dunn M, Wang D-P, Rossby HT, Benway RL. A study of the currents of the outer shelf and upper slope from a decade of shipboard ADCP observations in the Middle Atlantic Bight. J Geophys Res. 2006; 111:C06003.doi: 10.1029/2005JC003116

Ford WL, Longard JR, Banks RE. On the nature, occurrence and origin of cold, low salinity water along the edge of the Gulf Stream. J Mar Res. 1952; 11:281–293.

Fratantoni PS, Pickart RS, Torres DJ, Scott S. Mean structure and dynamics of the Shelfbreak Jet in the Middle Atlantic bight during fall and winter. J Phys Oceanogr. 2001; 31:2135–2156.

Garfield NW III, Evans DL. Shelf water entrainment by Gulf Stream warm-core rings. J Geophys Res. 1987; 92(C12):13,003–13,012.

Garvine RW. Subtidal frequency estuary-shelf interaction: Observations near Delaware Bay. J Geophys Res. 1991; 96:7049–7064.

Geyer, WR., Chant, R. The physical oceanography processes in the Hudson River estuary. In: Levinton, JS., Valdman, JR., editors. The Hudson River Estuary. Cambridge Univ. Press; New York: 2006. p. 13-23.

Glenn S, et al. Biogeochemical impact of summertime coastal upwelling on the New Jersey Shelf. J Geophys Res. 2004; 109:C12S02.doi: 10.1029/2003JC002265

Greene C, Pershing A. Climate drives sea change. Science. 2007; 315:1084–1085. [PubMed: 17322049]

Griffin CG, Frey KE, Rogan J, Holmes RM. Spatial and interannual variability of dissolved organic matter in the Kolyma River, East Siberia, observed using satellite imagery. J Geophys Res. 2011; 116:G03018.doi: 10.1029/2010JG001634

Guo LD, Santschi PH, Warnken KW. Dynamics of dissolved organic carbon (DOC) in oceanic environments. Limnol Oceanogr. 1995; 40(8):1392–1403.

Hedges, JI. Why dissolved organic matter. In: Hansell, DA., Carlson, CA., editors. Biogeochemistry of Marine Dissolved Organic Matter. Academic Press; San Diego, Calif: 2002. p. 1-33.

Herrmann M, et al. Net ecosystem production and organic carbon balance of U.S. East Coast estuaries: A synthesis approach. Global Biogeochem Cycles. 2015; 29:96–111. DOI: 10.1002/2013GB004736

Hofmann E, et al. Eastern U.S. continental shelf carbon budget: Integrating models, data assimilation, and analysis. Oceanography. 2008; 21:86–104.

Hofmann EE, et al. Modeling the dynamics of continental shelf carbon. Annu Rev Mar Sci. 2011; 3:93–122.

Houghton RNW, Fairbanks RG. Water sources for Georges Bank. Deep Sea Res II. 2001; 48:95–114.

Hu J, Fennel K, Mattern JP, Wilkin J. Data assimilation with a local Ensemble Kalman Filter applied to a three-dimensional biological model of the Middle Atlantic Bight. J Mar Syst. 2012; 94:145–156. DOI: 10.1016/j.jmarsys.2011.11.016

Hung JJ, Chen C-H, Gong G-C, Sheu D-D, Shiah F-K. Distributions, stoichiometric patterns and cross-shelf exports of dissolved organic matter in the East China Sea. Deep Sea Res Part II. 2003; 50:1127–1145.

Jahnke, RA. Global synthesis. In: Liu, KK., et al., editors. Carbon and Nutrient Fluxes in Continental Margins: A Global Synthesis. Springer; Berlin: 2010. p. 597-616.

Johnson DR, Miller J, Schofield O. Dynamics and optics of the Hudson River outflow plume. J Geophys Res. 2003; 108(C10):3323.doi: 10.1029/2002JC001485

Joyce TM, Bishop JKB, Brown OB. Observations of offshore shelf-water transport induced by a warmcore ring. Deep Sea Res. 1992; 39:S97–S113.

Kim YY, Weatherly GL, Pietrafesa LJ. On the mass and salt budgets for a region of the continental shelf in the southern Mid-Atlantic Bight. J Geophys Res. 2001; 106(C12):31,263–31,282.

Korosov AA, Posdnyakov DV, Grassl H. Spaceborne quantitative assessment of dissolved organic carbon fluxes in the Kara Sea. Adv Space Res. 2012; 50:1173–1188.

Lentz SJ. Observations and a model of the mean circulation over the Middle Atlantic Bight continental shelf. J Phys Oceanogr. 2008; 38(6):1203–1221. DOI: 10.1175/2007JPO3768.1

Lillibridge JL III, Hitchcock G, Rossby T, Lessard E, Mork M, Golmen L. Entrainment and mixing of shelf/slope waters in the near surface Gulf Stream. J Geophys Res. 1990; 95(C8):13,065–13,087. DOI: 10.1029/JC095iC08p13065

Linder CA, Gawarkiewicz G. A climatology of the shelfbreak front in the Middle Atlantic Bight. J Geophys Res. 1998; 103(C9):18,405–18,423. DOI: 10.1029/98JC01438

Liu Q, Pan D, Bai Y, Wu K, Chen C-TA, Liu Z, Zhang L. Estimating dissolved organic carbon inventories in the East China Sea using remote-sensing data. J Geophys Res Oceans. 2014; 119:6557–6574. DOI: 10.1002/2014JC009868

López R, Del Castillo CE, Miller R, Salisbury J, Wisser D. Examining organic carbon transport by the Orinoco River using SeaWiFS imagery. J Geophys Res. 2012; 117:G03022.doi: 10.1029/2012JG001986

Mannino A, Russ ME, Hooker SB. Algorithm development for satellite-derived distributions of DOC and CDOM in the U.S. Middle Atlantic Bight. J Geophys Res. 2008; 113:C07051.doi: 10.1029/2007JC004493

Mannino A, Novak M, Hooker S, Hyde K, Aurin D. CDOM algorithm development and validation for the continental margin along the northeastern U.S. Remote Sens Environ. 2014; 152:576–602. DOI: 10.1016/j.rse.2014.06.027

Matsuoka A, Hooker SB, Bricaud A, Gentili B, Babin M. Estimating absorption coefficients of colored dissolved organic matter (CDOM) using a semi-analytical algorithm for southern Beaufort Sea waters: Application to deriving concentrations of dissolved organic carbon from space. Biogeosciences. 2013; 10:917–927. DOI: 10.5194/bg-10-917-2013

Meybeck M. Riverine transport of atmospheric carbon: Sources, global typology and budget. Water Air Soil Pollut. 1993; 70:443–463.

Mitchell, BG., Kahru, M., Wieland, J., Stramska, M. Determination of spectral absorption coefficients of particles, dissolved material and phytoplankton for discrete water samples. In: Mueller, JL.Fargion, GS., McClain, CR., editors. Ocean Optics Protocols for Satellite Ocean Color Sensor Validation. Goddard Space Flight Center; Greenbelt, Md: 2003. p. 39-64.NASA/TM-2003-211621/Rev4-Vol.IV

Muller-Karger FE, Varela R, Thunell R, Luerssen R, Hu C, Walsh JJ. The importance of continental margins in the global carbon cycle. Geophys Res Lett. 2005; 32:L01602.doi: 10.1029/2004GL021346

Najjar RG, Friedrichs MAM, Cai W-J. Report of The U.S. East Coast carbon cycle synthesis workshop, January 19–20, 2012. Ocean Carbon and Biogeochemistry Program and North American Carbon Program. 2012:34.

O'Reilly, JE., Evans-Zetlin, C., Busch, DA. Chapter 21. Primary production. In: Backus, RH., editor. Georges Bank. MIT Press; Cambridge, Mass: 1987. p. 220-233.

Rasmussen LL, Gawarkiewicz G, Owens WB, Lozier MS. Slope water, Gulf Stream, and seasonal influences on southern Mid-Atlantic Bight circulation during the fall-winter transition. J Geophys Res. 2005; 110:C02009.doi: 10.1029/2004JC002311

Rennie SE, Largier JJ, Lentz SJ. Observations of a pulsed buoyancy current downstream of Chesapeake Bay. J Geophys Res. 1999; 104(C8):18,227–18,240.

Rossby T, Benway RL. Slow variations in mean path of the Gulf Stream east of Cape Hatteras. Geophys Res Lett. 2000; 27:117–120.

Savidge DK. Wintertime shoreward near-surface currents south of Cape Hatteras. J Geophys Res. 2002; 107(C11):3205.doi: 10.1029/2001JC001193

Savidge DK, Austin JA. The Hatteras Front: August 2004 velocity and density structure. J Geophys Res. 2007; 112:C07006.doi: 10.1029/2006JC003933

Savidge DK, Bane JM Jr. Wind and Gulf Stream influences on along-shelf transport and off-shelf export at Cape Hatteras, North Carolina. J Geophys Res. 2001; 106(C6):11,505–11,527.

Savidge DK, Savidge WB. Seasonal export of South Atlantic Bight and Mid-Atlantic Bight shelf waters at Cape Hatteras. Cont Shelf Res. 2014; 74:50–59.

Savidge DK, Austin JA, Blanton BO. Variation in the Hatteras Front density and velocity structure Part1: High resolution transects from three seasons in 2004–2005. Cont Shelf Res. 2012; doi: 10.1016/j.csr.2012.11.005

Schollaert S, Rossby T, Yoder J. Gulf Stream cross-frontal exchange: Possible mechanisms to explain interannual variations in phytoplankton chlorophyll in the Slope Sea during the SeaWiFS years. Deep Sea Res II. 2004; 51:173–188.

Sharp JH, Yoshiyama K, Parker AE, Schwartz MC, Curless SE, Beauregard AY, Ossolinski JE, Davis AR. A biogeochemical view of estuarine eutrophication: Seasonal and spatial trends and correlations in the delaware estuary. Estuaries Coasts. 2009; 32(6):1023–1043.

Signorini SR, Mannino A, Friedrichs M, Najjar R, Cai W-J, Salisbury J, Wang ZA, Thomas H. Surface ocean pCO_2 seasonality and sea-air CO_2 flux estimates for the North American East Coast. J Geophys Res Oceans. 2013; 118:5439–5460. DOI: 10.1002/jgrc.20369

Spencer RGM, Butler KD, Aiken GR. Dissolved organic carbon and chromophoric dissolved organic matter properties of rivers in the USA. J Geophys Res. 2012; 117:G03001.doi: 10.1029/2011JG001928

Stedmon CA, Markager S, Kaas H. Optical properties and signatures of Chromophoric Dissolved Organic Matter (CDOM) in Danish Coastal Waters. Estuarine Coastal Shelf Sci. 2000; 51:267–278. DOI: 10.1006/ecss.2000.0645

Valle Levinson A, Li C, Royer TC, Atkinson LP. Flow patterns at the Chesapeake Bay entrance. Cont Shelf Res. 1998; 18:1157–1177.

Verity, PG., Lee, TN., Yoder, JA., Paffenhöfer, G-A., Blanton, JO., Alexander, CR. Outer shelf processes. In: Menzel, D., editor. Ocean Processes: US Southeast Continental Shelf. DOE Office of Sci. and Tech. Inf.; OakRidge, Tenn: 1993. p. 45-74.

Verity PG, Bauer JE, Flagg CN, DeMaster DJ, Repeta DJ. The Ocean Margins Program: An interdisciplinary study of carbon sources, transformations, and sinks in a temperate continental margin system. Deep Sea Res. 2002; 49:4273–4295.

Vlahos P, Chen RF, Repeta DJ. Dissolved organic carbon in the Middle Atlantic Bight. Deep Sea Res Part II. 2002; 49:4369–4385.

Vodacek A, Blough NV, DeGrandpre MD, Peltzer ET, Nelson RK. Seasonal variation of CDOM and DOC in the Middle Atlantic Bight: Terrestrial inputs and photooxidation. Limnol Oceanogr. 1997; 42:674–686.

Walsh JJ. Particle export at Cape Hatteras. Deep Sea Res Part II. 1994; 41:603–628.

Wilkin JL, Hunter EJ. An assessment of the skill of real-time models of Mid-Atlantic Bight continental shelf circulation. J Geophys Res Oceans. 2013; 118:2919–2933. DOI: 10.1002/jgrc.20223

Zavala-Garay, J., Wilkin, J., Levin, J. Data assimilation in coastal oceanography: IS4DVAR in the Regional Ocean Modeling System (ROMS). In: Blayo, E., Bocquet, M., editors. Advanced Data Assimilation for Geosciences. Oxford Univ. Press; Oxford, U. K.: 2012.

Zhang W, Wilkin J, Arango H. Towards an integrated observation and modeling system in the New York Bight using variational methods, Part I: 4DVAR data assimilation. Ocean Modell. 2010; 35:119–133. DOI: 10.1016/j.ocemod.2010.08.003

Key Points

- Retrieved DOC from satellite CDOM within estuaries and shelf waters
- Computed stocks and lateral fluxes of DOC with satellite data and model physics
- Shelf fluxes of DOC are considerably higher than prior estimates

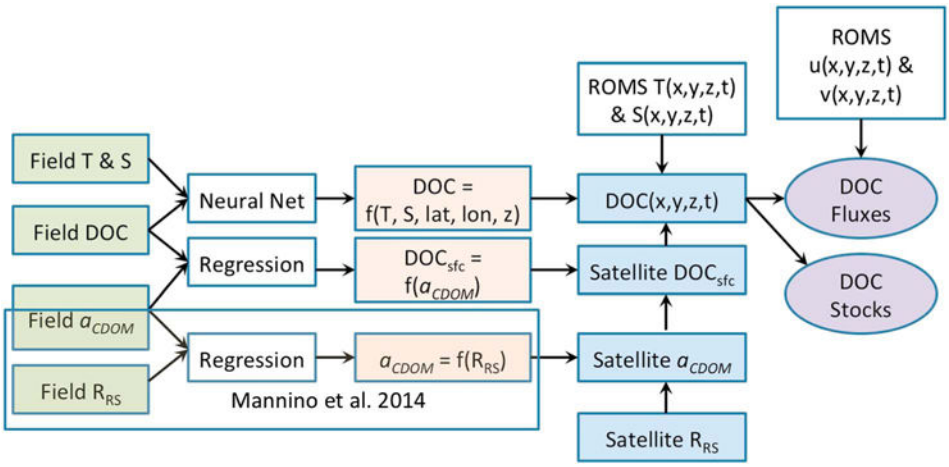

Figure 1.

Flow diagram illustrating the process for computing DOC stocks and fluxes. T = temperature, S = salinity, DOC = dissolved organic carbon, DOC_{sfc} = surface DOC, a_{CDOM} = CDOM absorption coefficient, R_{RS} = remote sensing reflectance, the $T(x, y, z, t)$ and $S(x, y, z, t)$ notations refer to the four-dimensional temperature and salinity fields from the ROMS model, and $u(x, y, z, t)$ and $v(x, y, z, t)$ represent the model velocity components. The shaded portion in the lower left shows the development of the a_{CDOM} satellite algorithms from *Mannino et al.* [2014].

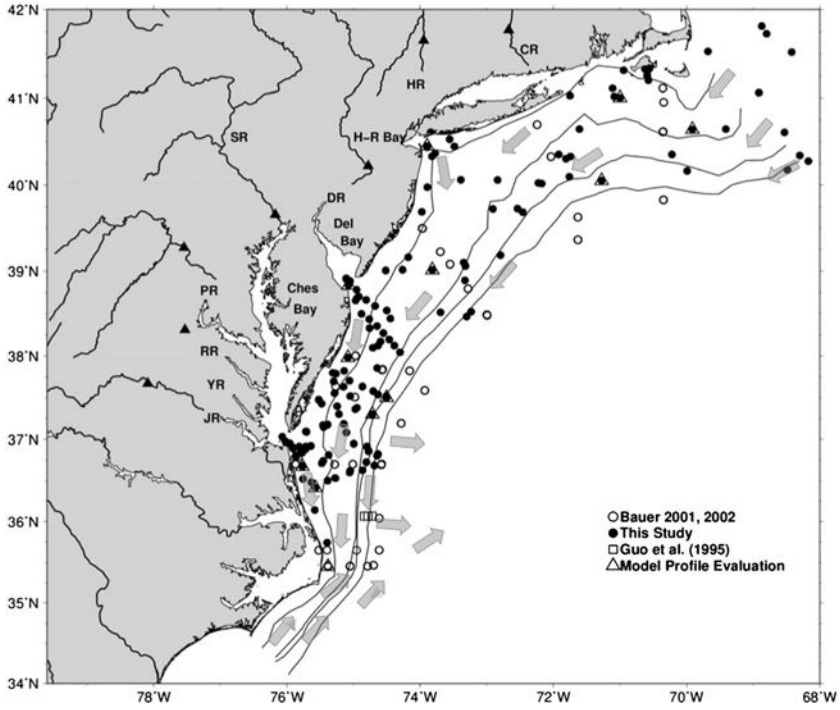

Figure 2.

Study site and station locations of field data used to train the neural networks model. The legend denotes the symbols for each of the data sets used. Model Profile Evaluation represents the locations for the DOC vertical profiles used in model development and evaluation. The arrows represent the major surface currents described in section 2.1. The major rivers that flow into estuaries and the MAB are shown along with the downstream USGS streamflow gauge locations (closed triangles): Connecticut River (CR), Hudson River (HR), Delaware River (DR), Susquehanna River (SR), Potomac River (PR), Rappahannock River (RR), York River (YR), and James River (JR).

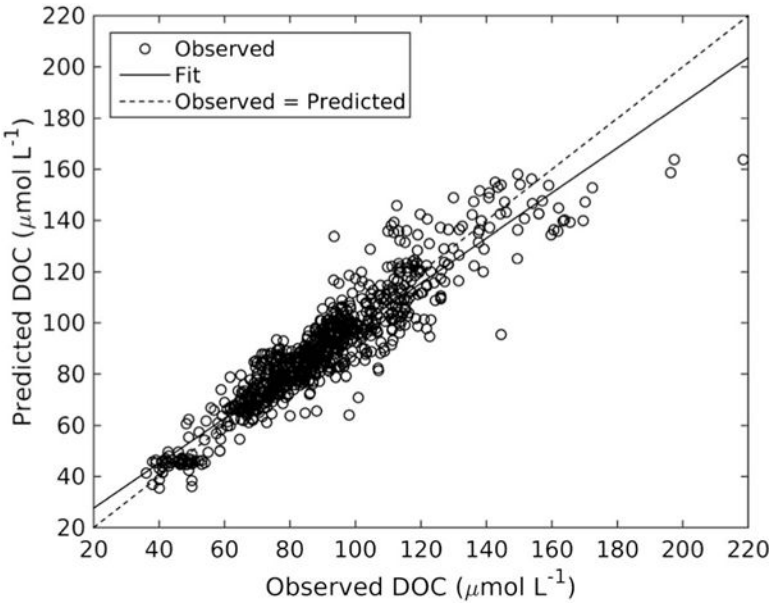

Figure 3.

Performance of the neural networks model showing predicted versus observed DOC concentration. Trend line: $Y = 0.87 \times$ observed DOC + 11; $R^2 = 0.882$.

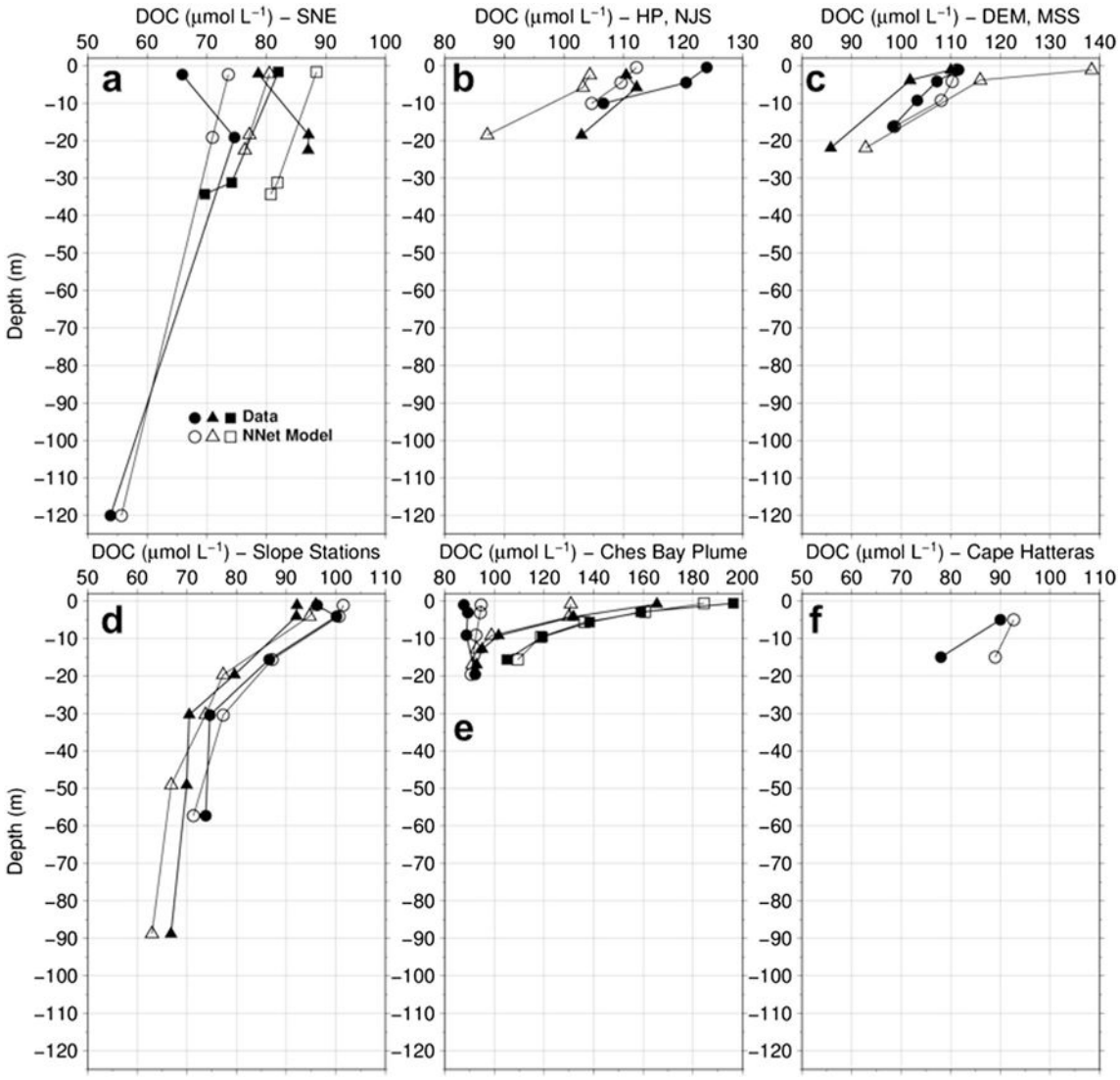

Figure 4.

Profiles of field data versus predicted DOC retrieved from the neural networks model for stations locations indicated on the map in Figure 2: (a) southern New England, (b) Hudson River plume and New Jersey shelf, (c) Delaware Bay mouth and midshelf, (d) slope stations from the southern MAB, (e) Chesapeake Bay plume, and (f) near Cape Hatteras. The neural net DOC profiles shown are derived strictly from input parameters of field observations of temperature, salinity, latitude, and longitude and shown to demonstrate the ability of the neural net to represent the vertical profile of DOC from input parameters.

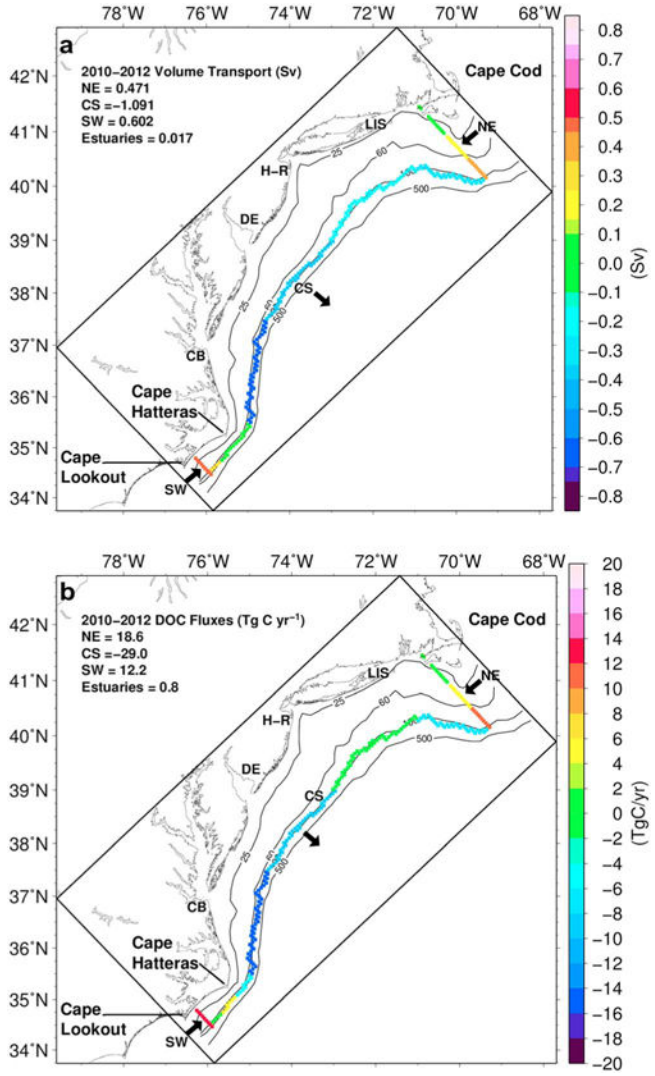

Figure 5.

Map of the ESPreSSO model domain for the MAB region with the mean annual (a) water volume transport in Sverdrups (10^6 m^3 s^{-1}) and (b) DOC fluxes (Tg C yr^{-1}) for 2010–2012 along the northeast boundary near Cape Cod (NE), southwest boundary located south of Cape Hatteras (SW), and cross shelf boundary along the 100 m isobath (CS). Positive values indicate flux into the MAB and negative values flux out of the MAB. The CS boundary was divided into five segments along the 100 m isobath at the SW, 35.5°N, 37.5°N, 39°N, 71°W (~40°N), and NE model grid cells for computation of regional water volume transport and DOC fluxes. The most southern segment was subdivided into three smaller sections as shown. Individual model grid cells (5–6 × 5–6 km) are shown along the boundary.

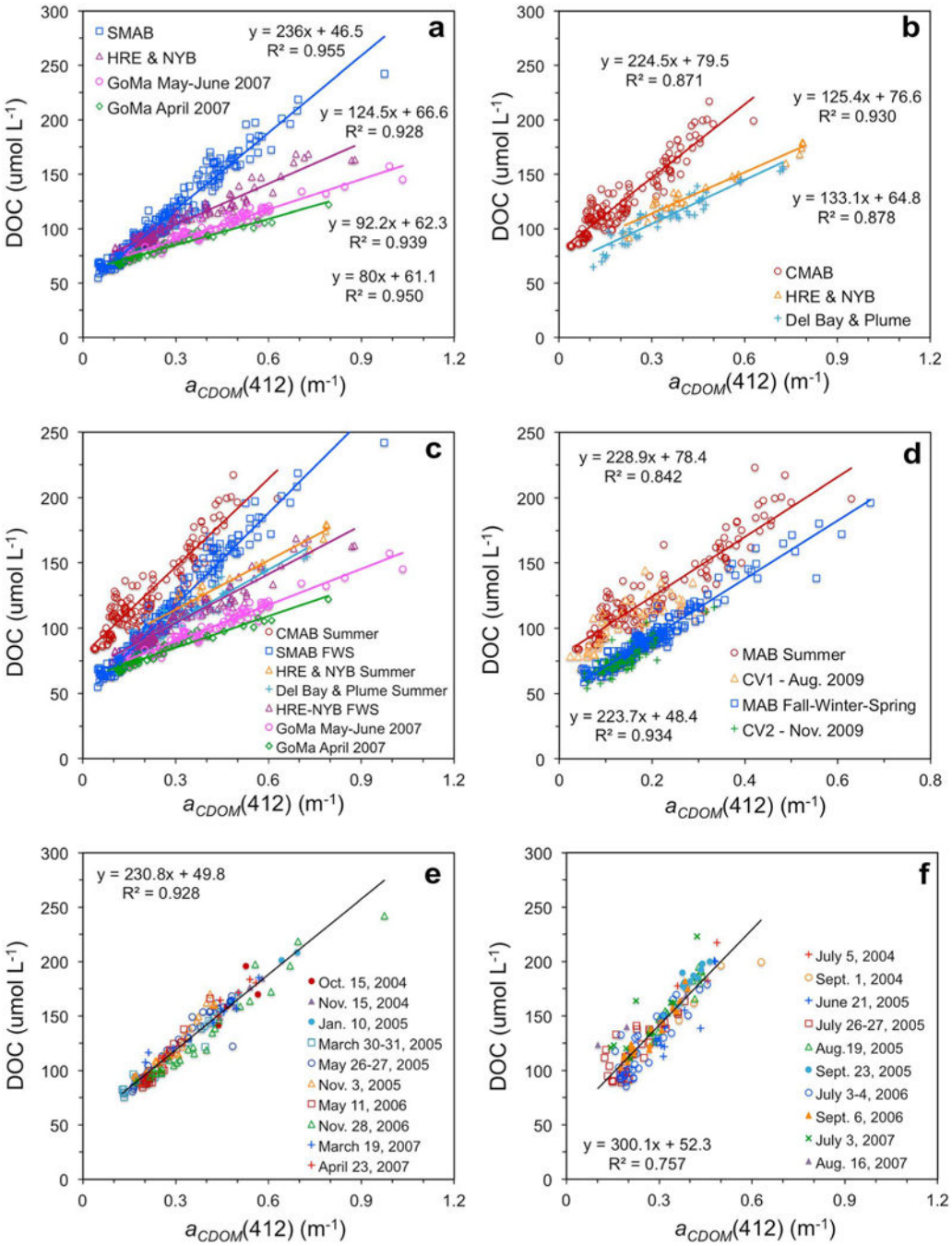

Figure 6.

Relationships of chromophoric dissolved organic matter (CDOM) absorption coefficient at 412 nm ($a_{CDOM}(412)$) with dissolved organic carbon (DOC) for (a) fall-winter-spring (FWS) in the Middle Atlantic Bight (MAB) and Gulf of Maine (GoMa); (b) summer MAB and GoMa; (c) combined FWS and summer in MAB and GoMa; (d) merged MAB data with evaluation data from CV1 and CV2 cruises; (e) FWS Chesapeake Bay lower estuary, mouth, and plume; and (f) summer Chesapeake Bay lower estuary, mouth, and plume. SMAB = Southern MAB, HRE = Hudson River Estuary, NYB = New York Bight, CMAB =

Chesapeake MAB, which represents the Chesapeake Bay lower estuary, mouth, plume, and adjacent shelf waters; Del Bay and Plume = lower Delaware Bay estuary, mouth, and plume.

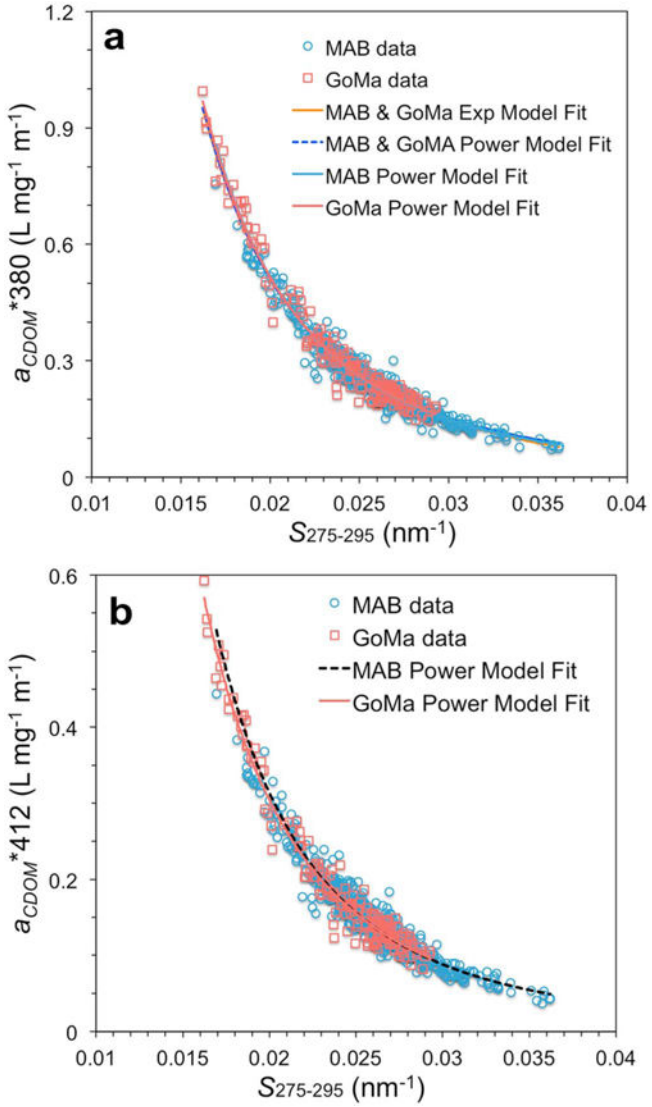

Figure 7.

Nonlinear power and exponential relationships of MAB and GoMA CDOM spectral slope ($S_{275–295}$) with the specific CDOM absorption coefficient at (a) 380 nm (a_{CDOM}*380) and (b) 412 nm (a_{CDOM}*412) from all seasons. a_{CDOM}*(380) = $\underline{a}_{CDOM}$(380)/DOC.

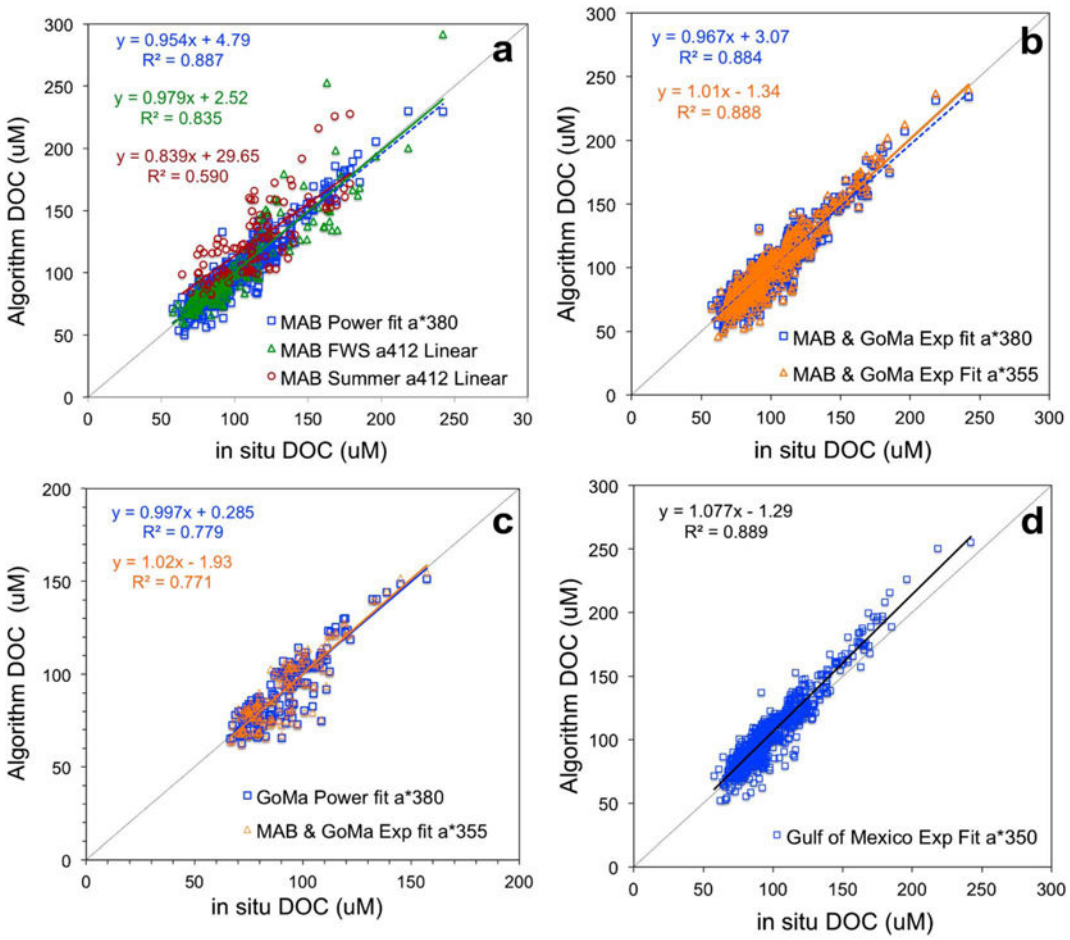

Figure 8.

Comparison of algorithm-derived DOC versus in situ DOC. The algorithms are based on in situ measurements of a_{CDOM} and DOC (a) MAB power a_{CDOM}*380 model and seasonal linear a_{CDOM}(412) for MAB data only, (b) MAB and GoMa a_{CDOM}*380 and a_{CDOM}*355 exponential models for MAB and GoMa data, (c) GoMa power a_{CDOM}*380 model and MAB and GoMa a_{CDOM}*355 exponential model for GoMa data only, and (d) exponential a_{CDOM}*350 model developed for the northern Gulf of Mexico by *Fichot and Benner* [2012] applied to MAB and GoMa data.

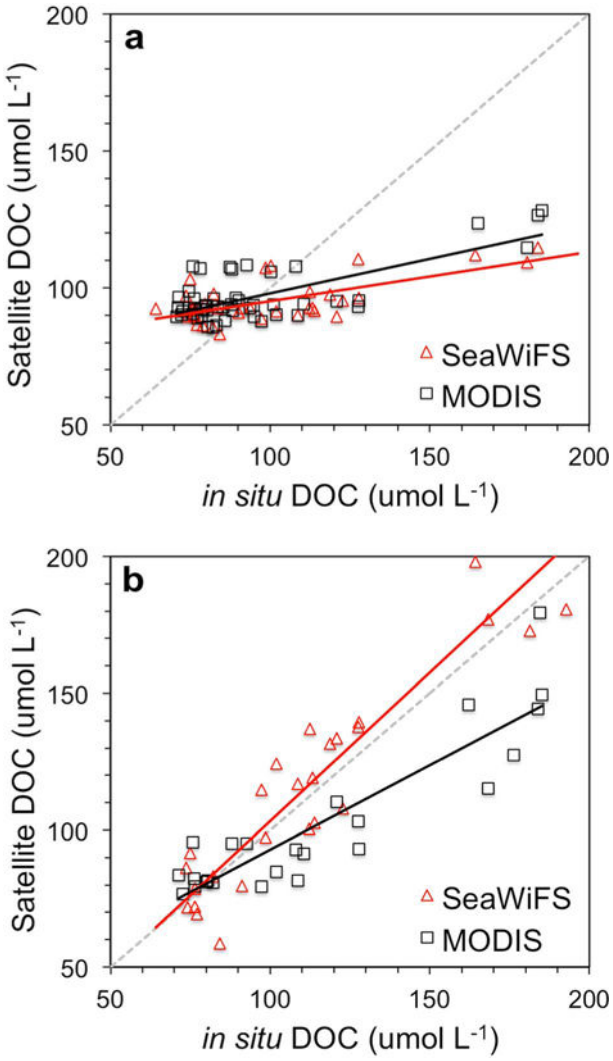

Figure 9.

Validation matchups of in situ DOC and MODIS Aqua and SeaWiFS DOC derived from the (a) exponential a_{CDOM}*(380) and (b) linear a_{CDOM}(412) DOC algorithms.

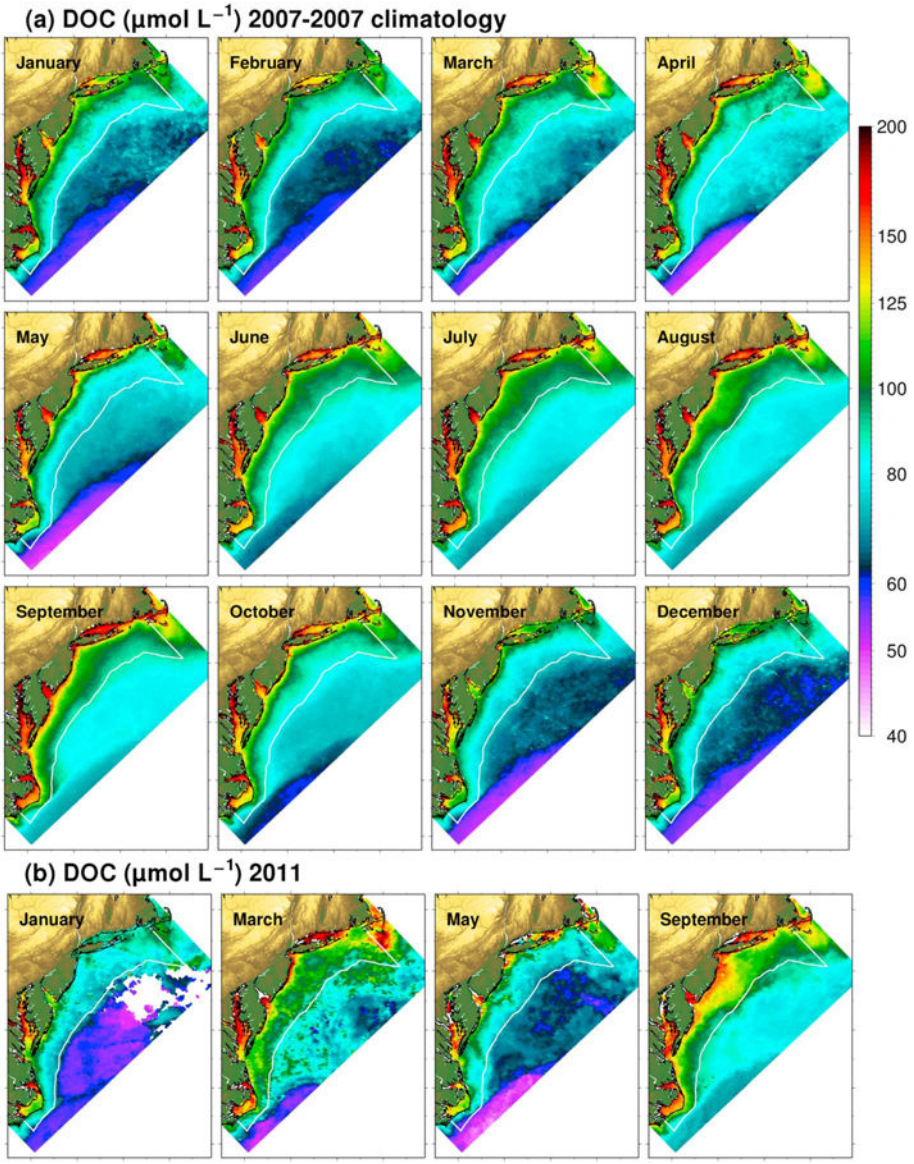

Figure 10.

Monthly MODIS Aqua distributions of near-surface (a) DOC climatology based on seven years of data (2006–2012) and (b) DOC for January, March, May, and September 2011.

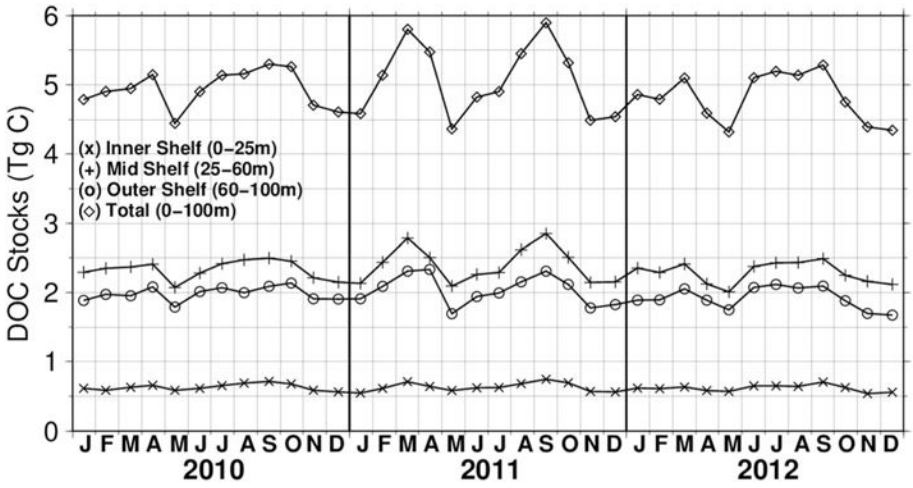

Figure 11.

MAB monthly integrated DOC stocks (Tg C) for 2010, 2011, and 2012. Time series are given for the inner, middle, and outer shelves, as well as the time series for the entire shelf.

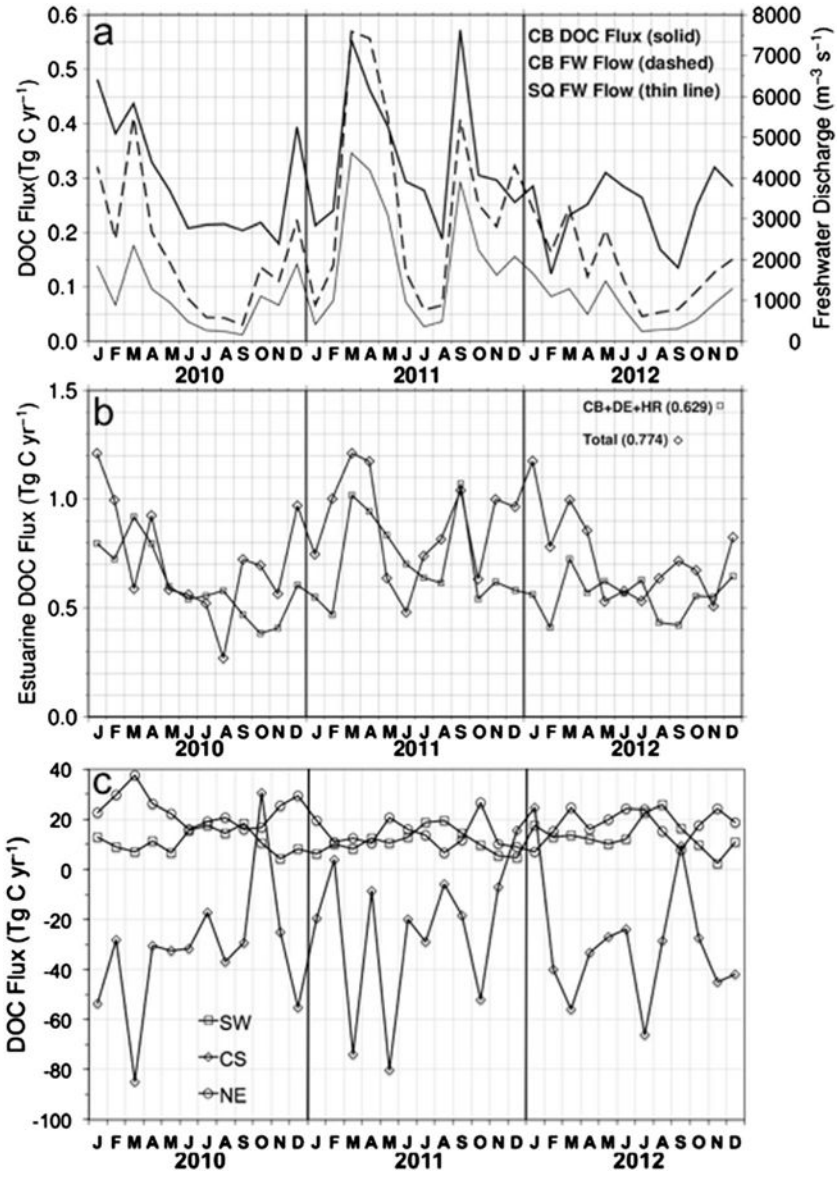

Figure 12.

Time series of (a) DOC flux and freshwater (FW) discharge at the mouth of Chesapeake Bay (CB) and from the Susquehanna River (SQ) at Conowingo Dam (USGS); (b) estuarine DOC flux total for the MAB and summed CB, Delaware Estuary (DE), and Hudson-Raritan Estuary (HR); and (c) MAB boundary DOC fluxes along the SW, NE, and cross shelf along the 100 m isobath.

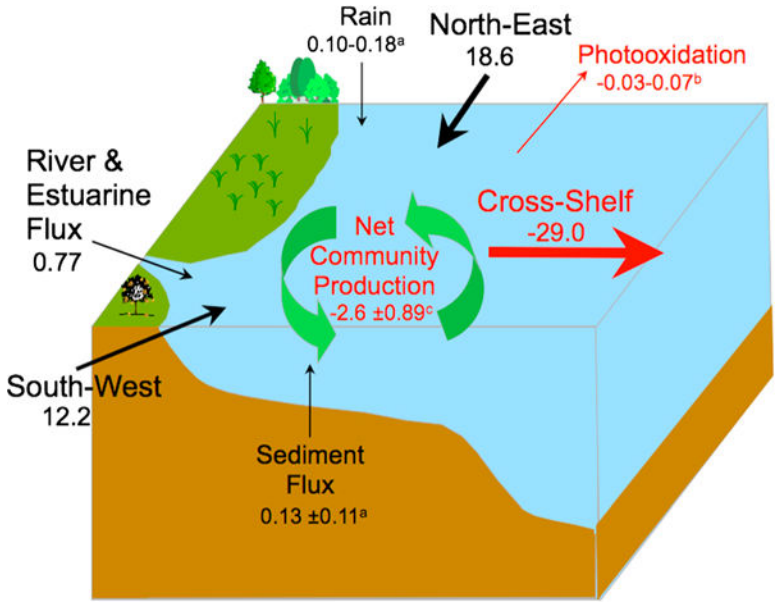

Figure 13.

DOC budget for the Middle Atlantic Bight. All units in Tg C yr^{-1}. (a) Values from *Vlahos et al.* [2002]; (b) values from *Del Vecchio et al.* [2009]; (c) the net community production (NCP) estimated is negative indicating external subsidies of DOC to the MAB (DOC respiration exceeds in situ production).

Table 1

Coefficients and Goodness-of-Fit Parameter Values of DOC Algorithms Retrieved From CDOM Properties[a]

	Power a_{CDOM}*(380) MAB and GoMa	Exponential a_{CDOM}*(380) MAB and GoMa	Exponential a_{CDOM}*(355) MAB and GoMa	Linear a_{CDOM}(412) MAB	
Equation	$Y = A \times X^B$	$Y = e^{(A - B \times X)} + e^{(C - D \times X)}$		$Y = A \times X + B$	
X =	$S_{275–295}$	$S_{275–295}$	$S_{275–295}$	$\ln(a_{CDOM}412)$	
Y =	a_{CDOM}*(380)	a_{CDOM}*(380)	a_{CDOM}*(355)	1/DOC	
	$\mathrm{DOC}=a_{\mathrm{CDOM}}380(A \times S_{275-295}{}^{B})$	DOC = $a_{CDOM}380/e^{(A - B \times S275–295)} + e^{(C - D \times S275–295)}$	DOC = $a_{CDOM}355/e^{(A - B \times S275–295)} + e^{(C - D \times S275–295)}$	DOC = $1/(A \times \ln(a_{CDOM}412) + B)$	
		Coefficients		Fall-Winter-Spring	Summer
A	4.357E−06	1.178	1.082	−0.004649	−0.002613
B	−2.983	103.6	87.25	0.003305	0.003771
C		4.237	3.859		
D		326.8	259.7		
		Goodness of Fit			
R^2	0.964	0.964	0.961	0.899	0.804
RMSE	0.0258	0.0258	0.0404	0.00073	0.00082
n	647	647	647	241	138

[a] aCDOM*(380) and aCDOM*(355) are the specific absorption coefficients and computed as aCDOM380/DOC and aCDOM355/DOC, respectively, with DOC in units of mg L^{-1} [e.g., *Blough and Del Vecchio*, 2002]. R^2 is the regression coefficient. RMSE represents the root-mean-square error (in units of the Y axis variable), and n is the sample size. MAB refers to algorithms developed only with field measurements from the Middle Atlantic Bight and MAB, and GoMa refers to algorithms developed with data from both the MAB and GoMa. The solutions of the equations for computing DOC are listed in the table. For the linear aCDOM412 algorithms, Fall-Winter-Spring refers to 1 November to 15 May and Summer refers to 16 June 16 to 30 September and a linear weighting function is applied for the transition periods in between these periods, 16 May to 15 June and 1–31 October. The cross symbol is used to represent the multiplication operator instead of asterisk to avoid confusion with the CDOM specific absorption notation.

Table 2

Coefficients and Goodness-of-Fit Parameter Values of DOC Algorithms Retrieved From $a_{CDOM}(412)$ for Estuarine Flux Computations[a]

	Linear $a_{CDOM}(412)$ Chesapeake Bay Mouth and Plume		Linear $a_{CDOM}(412)$ Delaware Bay Mouth and Plume		Linear $a_{CDOM}(412)$ Hudson-Raritan Estuary Mouth and Plume	
			Coefficients			
	Fall-Winter-Spring	Summer	Fall-Winter-Spring[b]	Summer	Fall-Winter-Spring	Summer
A	−0.004904	−0.002623	−0.004914	−0.004061	0.003388	0.003385
B	0.002615	0.003539	0.002795	0.004683	0.005460	0.004804
			Goodness of Fit			
R^2	0.925	0.866	0.942	0.859	0.920	0.899
RMSE	0.000575	0.000715	0.00071	0.00076	0.00047	0.000459
n	168	71	287	54	134	24

[a]Linear $a_{CDOM}(412)$ equation is the same as in Table 1. See Table 1 for further details. Fall-Winter-Spring refers to 15 October to 31 May, and Summer refers to 16 June to 30 September and a linear weighting function is applied for the transition periods in between these periods, 1–15 June and 1–14 October.

[b]Regional algorithm for DOC from the southern MAB region between 36° to 39°N.

J Geophys Res Biogeosci. Author manuscript; available in PMC 2017 November 29.

Table 3

Satellite Validation Statistics of DOC Algorithms Within the MAB[a]

Algorithm	MAPD (%)	±sd (%)	RMSE (μmol L^{-1})	Median Ratio	SIQR	Bias (%)	Slope	R^2	*n*
			SeaWiFS						
Power a_{CDOM}*(380)	18.1	10.9	25.1	0.99	0.180	−6.2	0.20	0.39	36
Exponential a_{CDOM}*(355)	18.7	11.3	24.7	1.04	0.185	−3.0	0.18	0.42	36
Exponential a_{CDOM}*(380)	18.0	11.1	25.0	1.02	0.181	−4.8	0.18	0.44	36
Linear a_{CDOM}(412)	11.1	7.5	15.2	1.05	0.091	9.0	1.09	0.90	28
			MODIS						
Power a_{CDOM}(380)	17.2	10.9	22.3	1.08	0.138	0.60	0.27	0.46	50
Exponential a_{CDOM}*(355)	18.8	11.4	23.0	1.11	0.130	3.7	0.24	0.48	50
Exponential a_{CDOM}*(380)	17.4	10.9	22.3	1.08	0.127	1.7	0.25	0.52	50
Linear a_{CDOM}(412)	13.9	9.2	18.0	1.04	0.100	−0.9	0.57	0.76	35

[a] sd is the standard deviation of the MAPD. SIQR is the semi-interquartile range. The slope and R^2 values are from Type II (Deming) linear regression analysis of 1-to-1 matchups between satellite DOC versus in situ DOC values. Linear CDOM algorithms were seasonally weighted via linear interpolation for transition periods.

Table 4

Satellite DOC Areal Averages (μmol L^{-1} C) for the Three Shelf Boundaries and All Estuary Boundary Pixels Combined

Year	Estuaries	SW	NE	CS
2010	112.3	73.1	89.9	70.5
2011	112.0	71.3	93.4	71.1
2012	111.5	67.8	86.9	68.4
Mean	111.9	70.7	90.1	70.0

Table 5

DOC Flux Estimates (Tg C yr^{-1}) for All Combined Estuaries and the Three Continental Shelf Boundaries[a]

Year	Estuaries	SW	NE	CS
2010	0.72 (0.30, 1.22)	11.4 (8.8, 14.9)	23.6 (17.7, 30.6)	32.9 (27.6, 38.6)
2011	0.87 (0.37, 1.48)	11.2 (8.4, 14.7)	14.1 (10.0, 18.9)	24.6 (20.4, 29.2)
2012	0.73 (0.31, 1.24)	13.9 (9.8, 18.6)	18.0 (14.1, 22.6)	29.6 (25.6, 34.0)
Mean	0.77 (0.33, 1.31)	12.1 (9.0, 16.1)	18.5 (13.9, 24.0)	29.0 (24.5, 33.9)

[a]The cross-shelf (CS) flux is negative indicating that the flux is out of the shelf domain, while all the other fluxes are positive, indicating fluxes into the shelf. The values between parentheses correspond to the 95% confidence interval. The mean volume transport in sverdrups (10^6 m^3 s^{-1}) and standard deviation (based on monthly mean values) for all MAB estuaries and the SW, NE, and CS shelf boundaries are, respectively, 0.017 ± 0.005, 0.474 ± 0.173, 0.603 ± 0.246, and 1.09 ± 1.07.

Table 6

Water Volume Transport for the MAB Region

Region/Boundary Flow (Sv)	Flow (Sv)	References
		Southward Alongshore
Cape Cod (125 m)	0.64	*Lentz* [2008]; cross-shelf transects from coast to water depth listed
Northeast	0.46 ± 0.32	*Fratantoni et al.* [2001]
Northeast	0.4	*Beardsley and Boicourt* [1981] (cited in *Biscaye et al.* [1994] and *Vlahos et al.* [2002])
Northeast	0.6	*Flagg* [1977] (cited in *Biscaye et al.* [1994])
39.5–41.5°N shelf break jet	0.45	*Linder and Gawarkiewicz* [1998]
39–41°N shelf break jet	0.24	
37–39.5°N shelf break jet	0.16	
Shelf break jet at ~39.8°N	0.4	*Flagg et al.* [2006]
South of 38°N (0–100 m bathymetry)	0.124	*Biscaye et al.* [1994]
Northeast to ~35.3°N	0.3	*Beardsley et al.* [1976] and *Beardsley and Boicourt* [1981] (cited in *Churchill and Berger* [1998])
~36.7°N	0.15 ± 0.07	*Kim et al.* [2001]
35.5–36.5°N: shelf water	0.025	*Churchill and Gawarkiewicz* [2009]
Shelf break front	0.4	
Hatteras Front (~35°N)	0.048	*Savidge and Austin* [2007]
NE	0.60	ESPreSSO 2010–2012
		Northward Alongshore
SW	0.24	*Savidge and Bane* [2001]
SW (20–60 m isobaths)	0.09	*Savidge and Savidge* [2014]
SW	0.1	*Flagg* [1977] and *Beardsley and Boicourt* [1981] (cited in *Vlahos et al.* [2002])
SW	0.47	ESPreSSO 2010–2012
Cross Shelf		
37.5–38°N: shelf break front	−0.7 to 1.3	*Rasmussen et al.* [2005]
North and South of Cape Hatteras	+ (Into MAB)	*Churchill and Cornillon* [1991], *Churchill* and *Berger* [1998], and *Savidge* [2002]
Near Cape Hatteras	−0.24	*Savidge and Bane* [2001]
South of Cape Hatteras	−0.15	
~35.33–35.67°N	−0.09	*Churchill and Berger* [1998]
~35.5°N (southeast)	−0.081	*Kim et al.* [2001]
~36.5°N (eastward)	−0.063	
Gulf Stream filament	−0.8 to −0.9	*Joyce et al.* [1992]
MAB Gulf Stream eddies	−0.13	*Churchill et al.* [1993]
Gulf Stream filaments ~35.8–37.2° N	−0.1 to −0.5	*Lillibridge et al.* [1990]
MAB	−0.3	*Flagg* [1977] and *Beardsley and Boicourt* [1981]
At Cape Hatteras	−0.2	(cited in *Vlahos et al.* [2002])
MAB	−1.09	ESPreSSO 2010–2012 (see Figure 4a)
		Estuary Shelf
Chesapeake Bay	0.008	*Valle Levinson et al.* [1998]
Delaware Bay	0.002	*Garvine* [1991]

Region/Boundary Flow (Sv)	Flow (Sv)	References
Hudson-Raritan Estuary	0.001	*Geyer and Chant* [2006]
MAB total	0.005	*Beardsley and Boicourt* [1981] (cited in *Vlahos et al.* [2002])
Chesapeake Bay	0.006	ESPreSSO 2010–2012
Delaware Bay	0.0076[a]	ESPreSSO 2010–2012
Hudson-Raritan Estuary	~0	ESPreSSO 2010–2012
MAB total	0.017	ESPreSSO 2010–2012

[a]The Delaware Bay water volume transport and thus DOC flux at the bay mouth are significantly overestimated by the approach implemented using ESPreSSO model output. An ongoing study with a higher-resolution model of Delaware Bay reveals water transport values at the mouth to be closer to the value reported by *Garvine* [1991].